J Mater Sci: Mater Electron (2016) 27:12729–12763
DOI 10.1007/s10854-016-5407-3

Recent progress of Sn–Ag–Cu lead-free solders bearing alloy elements and nanoparticles in electronic packaging

Jie Wu[1] · Song-bai Xue[1] · Jing-wen Wang[1] · Shuang Liu[1] · Yi-long Han[1] · Liu-jue Wang[1]

Received: 20 April 2016 / Accepted: 20 July 2016 / Published online: 23 July 2016
© Springer Science+Business Media New York 2016

Abstract Sn–Ag–Cu lead-free solders, containing alloy elements and nanoparticles, have been extensively investigated. With the extensive prevalence of 3D IC package, a major concern of Sn–Ag–Cu based solders today is continuously focused on extending service life of solder bonding formed between solders and substrates. The critical issues and improvements on Sn–Ag–Cu solders bearing alloys and nanoparticles are outlined and evaluated in this review. It can be summarized that appropriate content of certain alloys or nanoparticles addition to Sn–Ag–Cu solder is possible to tailor the solder properties, such as the melting and solidification behaviors, oxidation resistance, wettability, (interfacial) microstructure, and mechanical properties. Worthy of note is that reliability issues such as creep behavior, thermomechanical fatigue, electromigration, thermomigration and Sn whisker were briefly discussed and analyzed to lay down a solid foundation for the future development of 3D IC technology.

1 Introduction

In recent years, the utilization of conventional Sn–Pb solders in consumer electronic products have been extensively banned by correlative green initiatives of WEEE and RoHS due to the toxic and not environment-friendly substance (Pb) in it [1, 2]. So, several lead-free solders that can substitute Sn–Pb solders have been synthesized, mainly including Sn–Ag, Sn–Bi, Sn–Cu binary-system solders and Sn–Ag–Cu, Sn–Ag–Bi, Sn–Cu–Ni, Sn–Zn–Bi ternary-system solders [3, 4]. Among these alternative lead-free solders, Sn–Ag–Cu system solders are widely regarded as the most promising candidate to replace Sn–Pb solders for their comparatively favorable performance [5–7]. Unfortunately, when compared with traditional Sn–Pb solders, Sn–Ag–Cu lead-free solders still have a mount of limitations, such as higher melting temperature (T_m, 217–221 °C), relatively poor wettability, bulk intermetallic compounds (IMCs) growth and unsatisfactory mechanical strength [8–11]. Besides, as the electronic packages get more complex in geometry and material properties, solder bonding subjected to wretched service conditions (e.g., corrosive environment, isothermal aging, drop impact, radiation) deserves considerable concerns [12–14]. Therefore, there is a continuous interest to better understand and optimize the morphology of interfacial IMC layer with a proper thickness for its determination in the reliability of solder joint [15, 16]. Moreover, with the extensive prevalence of 3D IC packaging, the coupling effects of electromigration (EM) and thermomigration (TM) induced by high current density on micro-bumps become more severe, thus evidently shortening the service life of electronic devices. So, some reliability evaluations are pretty essential to be established to early estimate the service life of the micro-bumps subjected to the coupling effects of EM or TM [17, 18]. Apart from issues associated with basic properties and reliability, cost is another noteworthy shortage for large-scale applications of Sn–Ag–Cu solders due to the existence of valuable and expensive metal (Ag) [19, 20]. Even more serious is that these referred-above property deficiencies and reliability issues might be somewhat aggravated when the Ag concentration in Sn–Ag–Cu solders is intentionally reduced [21–23]. In order to

✉ Song-bai Xue
xuesb@nuaa.edu.cn

[1] College of Materials Science and Technology, Nanjing University of Aeronautics and Astronautics, Nanjing 210016, People's Republic of China

overcome these property degradation and reliability issues, trace amount of alloys (e.g., rare earth (RE), In, Bi, Ni, Ga, Al) are selected to be manually fused into Sn–Ag–Cu solders, which have also been widely demonstrated as an effective approach to further enhance the comprehensive performance of Sn–Ag–Cu solders [24, 25]. However, RE addition may in reverse encourage Sn whisker growth when added excessively into Sn–Ag–Cu solders, which is a potential reliability risk to trigger a short circuit and even result in a catastrophic event [26, 27].

Nowadays, the extensive popularity of nanotechnology is gradually arousing general research interest worldwide for particles with size down to nanometer observed series of specific properties emerging. So, this hews out a brand new methodology to optimize relative properties of Sn–Ag–Cu solders, provided that these nano-particles can be successfully incorporated into solders [28, 29]. As expected, a mount of satisfactory modified results especially with regard to the mechanical enhancement and thermal stability can be obtained after various nanoparticles were introduced into Sn–Ag–Cu solders such as oxides (e.g., Al_2O_3, TiO_2), carbides (e.g., CNTs, SWCNTs, Ni–CNTs), or borides with relatively high melting temperature (2000–3000 °C) [30–34]. But, research on nanoparticles-doped Sn–Ag–Cu solders is currently stay at the academic stage with no findings of applications in practical solder joint technology. After all, the basic requirement for solder joints in circuit interconnects is to form metallurgical bonding with satisfactory electrical conduction and then the mechanical property concern [1, 35, 36].

The objective of this review is to outline the effects of adding various alloy elements and nanoparticles on the properties of Sn–Ag–Cu lead-free solders, including melting characteristics, oxidation resistance, wettability, microstructures, interfacial reactions, mechanical properties, creep resistance, reliability, etc. In particular, the influences of electric potential and thermal gradient induced by a relatively high current density on corresponding atom migration located at the solder joint are analyzed. At last, a noteworthy reliability issue—Sn whisker in excessive RE-containing solders is introduced and the in-depth investigations on their growth mechanisms are discussed as well.

2 Melting characteristics

The melting temperature (T_m) of a certain solder alloy is vitally important for its determination in the lower limit of soldering temperature. Besides, its upper limit is highly dependent on the thermal features of components and devices on board to protect the heat-sensitive parts in practical soldering process [37, 38]. With the substitution of Sn–Pb solder, a predominant problem that Sn–Ag–Cu solder encounters is its higher melting point (217 °C). So, lowering down the T_m of Sn–Ag–Cu solder to some level becomes particularly essential. Generally, this can be approached through felicitously fusing low-melting alloys (e.g., Ga [39], Bi [40], In [41], Zn [42, 43]) into original solder, as displayed in Table 1. It can be obtained that adding Zn (0–3 wt%) into Sn–1.0Ag–0.3Cu brings the most pronounced drop level (from 227.7 to 220.8 °C) in the melting point of original solder alloy, as illustrated in Fig. 1 [43]. As can be observed, after Zn addition, the two apparent steps during the melting procedure of original solder change into one step of melting, indicative of an accelerated solidification process. However, weeny alterations in the T_m of Sn–Ag–Cu solder were made by alloys such as Ni [42], Ti [44], Fe [45], RE (e.g., La, Ce, Pr, Nd) [46, 47]. So, conventional soldering parameters can be applied as usual when these novel solders are utilized to fabricate interconnects. Moreover, the T_m for particle-reinforced Sn–Ag–Cu solders couldn't be visibly altered either, even with the size of incorporated particles decreased down to a nano-scaled range (e.g., TiO_2 [30], ZnO [31], GNSs [48], Ni–CNTs [49], Ag-coated SWCNTs [50], SiC [51], Diamond (Dia) [29]). This is probably due to their minor amount of addition. However, Sn–Ag–Cu solders with a nanoscaled size synthesized through chemical reduction method [52] or electrodeposition method [53] witness an apparent decrease in melting point. This nanoscaled Sn–Ag–Cu solder with numerous specific advantages is now attracting more and more scientific and technological attention. But, to date, massive problems haven't been resolved in the links of production, storage and application [54, 55]. So, further efforts need to be inputted to broaden their application into electronic market.

Melting range (pasty range), defined as the difference between liquidus and solidus temperature (T_S and T_L), is another significantly important thermal parameter. Solders with low melting range exist as fractional liquid for a short period during solidification, making it possible to obtain reliable joints and further enhance the board-level drop-impact reliability, while those with too large melting range are strongly vulnerable to manufacturing issues, such as fillet lifting, porosity and hot tearing contraction [40, 43, 51, 56, 57]. Generally, there exist five approaches to narrow down the melting range of solders, including an increment in T_S but no shift in T_L (Type I), a decrement in T_L but no shift in T_S (Type II), a higher decrement in T_L than that in T_S (Type III), a higher increment in T_S than that in T_L (Type IV), a decrement in T_L but an increment in T_S (Type V), as shown in Fig. 2. However, considering an overall low-temperature melting process, we argue that "Type III" can best satisfy the practical soldering

Table 1 The effects of trace amount of elements and nanoparticles on the thermal parameters of Sn–Ag–Cu solder alloys

SAC/SAC-X solder	Solidus temp.T_S (°C)	Liquidus temp.T_L (°C)	Melting range.T_L-T_S (°C)	Melting temp.T_m (°C)	Undercooling. (°C)
SAC0507/SAC0507-0.05Ni [7]	212.0/211.4	224.6/223.3	12.6/11.9	221.1/222.9	9.8/6.3
SAC0507/SAC0507-1 Ga [39]	217/211.5	_	_	227.4/225.8	_
SAC103/SAC103-3Zn [43]	218.5/218.0	232.3/225.5	13.8/7.5	227.7/220.8	4.2/2.5
SAC105/SAC105-0.3Fe [45]	217.52/217.63	226.97/226.48	9.45/8.85	_	9.70/20.29
SAC105/SAC105-0.06Ni [56]	216.4/217.0	234.5/233.6	18.1/16.6	226.0/226.6	35.6/26.4
SAC105/SAC105-0.5Sb [56]	216.4/219.5	234.5/237.6	18.1/18.1	226.0/227.4	35.6/26.8
SAC157/SAC157-1.0Bi [40]	215.9/214.0	225.4/223.8	9.5/9.8	220.2/218.2	18.1/15.7
SAC205/SAC205-0.05Ni [42]	212.9/212.7	220.0/221.6	7.1/8.9	213.5/214.1	26.1/18.0
SAC205/SAC205-0.5Zn [42]	212.9/211.5	220.0/218.5	7.1/7.0	213.5/212.5	26.1/1.4
SAC305/SAC305-0.5Ni [58]	219.9/218.7	221.7/224.4	1.8/5.7	221.6/224.4	24.2/15.7
SAC355/SAC355-1Ti [44]	216.92/216.59	221.58/219.47	4.66/2.88	_	_
SAC105/SAC105-0.75SiC [51]	215.1/217.9	226.6/227.6	11.5/9.7	226.5/227.3	18.6/15.4
SAC305/SAC105-0.05TiO_2 [30]	216.4/216.6	217.7/219.1	1.3/2.5	217.7/219.1	_

"/" and "_" represent space character and no recorded data, respectively. SAC0507, SAC157, SAC205, SAC305 and SAC355 represent Sn–0.5Ag–0.7Cu, Sn–1.5Ag–0.7Cu, Sn–2.0Ag–0.5Cu, Sn–3.0Ag–0.5Cu, Sn–3.5Ag–0.5Cu, respectively

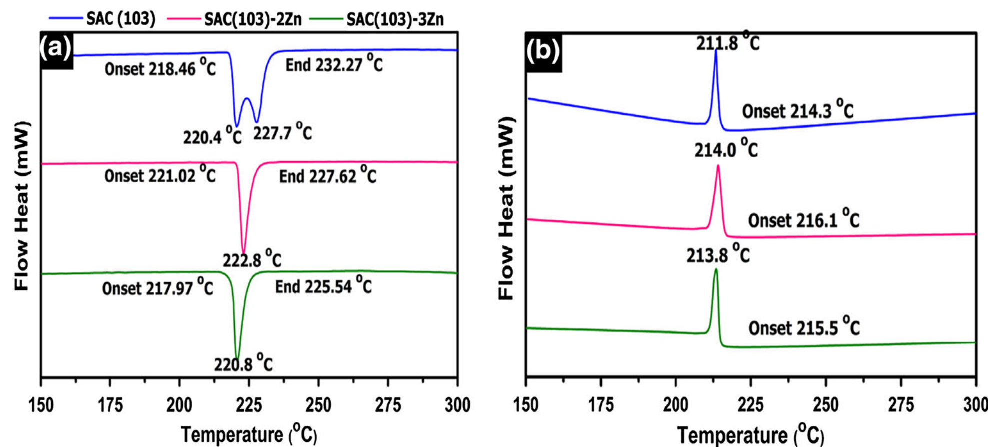

Fig. 1 DSC results of Sn–1.0Ag–0.3Cu–xZn (x = 0, 2, 3 wt%) solder alloys during **a** heating (endothermal) and **b** cooling (exothermal) process [43]

requirements among them. Accordingly, only alloys of Ni [7], Zn [42, 43], Ti [44] with appropriate content, as listed in Table 1, play a comparatively positive role in lowering the melting range of corresponding Sn–Ag–Cu solders. Whereas, Fe addition [45] does limited contribution to it because of tiny increment in solidus temperature (T_S). However, most additions are still acceptable given the melting range for eutectic Sn–Pb solder (11.5 °C) [57].

Undercooling is defined as the difference between the T_{onset} upon heating and the T_{onset} upon cooling in the DSC curve. Generally, the undercooling level is substantially determined by the preferentially formed solid phases in molten solder since these solid phases can serve as additional sites to accelerate the solidification process. Consequently, insufficient time will be left for relevant phases to grow up, which contributes to more refined structures that can evidently improve the mechanical properties of solder [7, 14, 58, 59]. For instance, almost all the alloys (except Fe [45]) and nanoparticles listed in Table 1 can lower the undercooling of corresponding Sn–Ag–Cu solders to

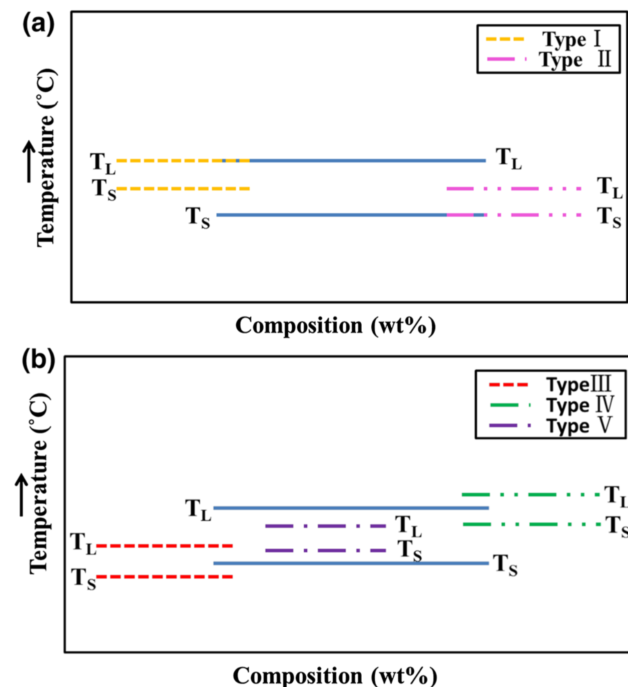

Fig. 2 Schematic diagrams of five approaches to narrow down the melting range of solder: **a** no shift in T_L or T_S, **b** shift both in T_L and T_S

different levels, particularly elemental Zn (0.5 wt%), which brought a pronounced decrement in the undercooling of Sn–2.0Ag–0.5Cu solder, from 26.1 to 1.4 °C. This was due to the substitution of Sn sites by Zn atoms and the preferentially formed IMCs (Cu_5Zn_8) in the solder matrix, both of which can serve as additional nucleation sites to activate the nucleation process on cooling. As a result, nearly all the visibly large Ag_3Sn precipitates vanished due to inadequate time to grow up, thereby benefiting the mechanical properties of solder. Similarly, it is the $(Cu,Ni)_6Sn_5$ IMCs primarily formed in Sn–2.0Ag–0.5Cu–0.05 Ni that accelerates the solidification process and finally avoids the emergence of obviously large Ag_3Sn [42]. Moreover, as for solders of Sn–1.5Ag–0.7Cu–1Bi and Sn–3.5Ag–0.5Cu–1Ti, the extra heterogeneous phases initiating the solidification process are identified to be Sn–Ti IMCs and Bi sites, respectively [14, 24, 40, 44]. However, few researches have investigated the influence of RE addition on the undercooling of Sn–Ag–Cu solders. It was presumed to be a suppressive effect as well since RE themselves or Sn–RE particles can provide additional nucleation sites for Sn phase which can accelerate the freezing sequence [3, 22, 25, 60]. As for refractory nanoparticles like SiC [51] with relatively high T_m, they will sacrifice themselves as additional nucleation sites to initiate the solidification process and finally achieve the goal of undercooling reduction.

3 Antioxidant property

The oxidation resistance of solders is one of the critical properties that should be considered seriously particularly over wave soldering to fabricate reliable interconnects for electronic packages. Since Sn–Ag–Cu solder has higher Sn concentration than that of traditional Sn–Pb solder, the oxidation susceptibility of Sn–Ag–Cu solder may get stronger [61, 62]. The common method to solve this oxidation issue was to introduce a certain fourth element (e.g., P, Ge, In, RE) into original solder to form a protective barrier, so that it can keep the molten solder isolate from air and thereby hindering the oxidation process. For instance, the antioxidant capacity of Sn–3.0Ag–0.5Cu solder with separate incorporation of Ni (0.1 wt%), P (0.01 wt%) and Ce (0.05 wt%) were compared by Dong et al. [63]. The comparative results revealed that solder containing 0.01 wt% P displayed a remarkable oxidation resistance due to the formation of a dense phosphorus-containing film ($SnO{\cdot}P_2O_5$, $4P + 5O_2 \rightarrow 2P_2O_5$; $SnO + P_2O_5 \rightarrow SnO \cdot P_2O_5$ [64]) on molten solder surface. So this dense phase provided possibility for the molten solder isolate from air, which was conducive to the subsequent wetting on Cu substrate. In addition, Fig. 3 [65] illustrates the thermo gravimetric analysis (TGA) results of oxidation characteristics of Zn- and Ge-containing Sn–3.0Ag–0.5Cu solder. As can be seen, Sn–3.0Ag–0.5Cu–1Ge solder exhibited the lowest weight gain in comparison to other tested samples. This is mainly because that a thin isolated GeO_x layer formed on the surface of liquid solder by Ge oxidation can effectively prevent air from reaching and oxidizing the molten solder. Moreover, adding elemental

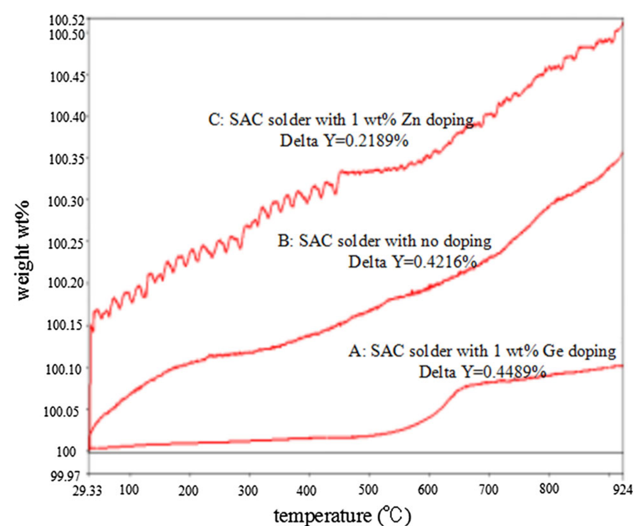

Fig. 3 Thermo gravimetric analysis (TGA) curve of solders (Sn–3.0Ag–0.5Cu, Sn–3.0Ag–0.5Cu–1Ge, Sn–3.0Ag–0.5Cu–1Zn) after high temperature oxidation (300 °C, 90 min) [65]

Into the Sn–2Ag–3Bi alloy could effectively inhibit Sn oxidation due to the tendency of In segregation on the surface of liquid solder, which could keep the molten solder away from the air [66]. Hence, it may prompt us to fuse elemental In into the Sn–Ag–Cu solder to explore its antioxidant capacity. However, RE addition does limited contribution to preventing molten solder from oxidation when compared with afore-mentioned alloys addition (e.g., P, Ge, In) due to their easier inclination to induce Sn whisker [67].

Besides, with lead-free nano-solders gradually emerging in electronic markets, solder oxidation issue gets more severe because of their unique qualities of large surface area per unit volume and large surface energy. Therefore, it's essential to develop new and specially synthesized surfactant that can not only avoid nanosolders oxidation and agglomeration, but also can be simply and completely removed during assembling process. For instance, Ref [55] reported with vapor phase flux assistance, the oxidation layer on lead-free nanosolder particles could be successfully removed. In addition, special passivation systems for protecting nanosolders from oxidation during storage were investigated by Novikov et al. [54] and the best protection function was obtained on silicon nitride. However, this passivation material is not appropriate to fabricate stable and homogenous solder joints. One possibility is to apply noble metals as passivation, such as gold or silver which are stable against the corrosion.

4 Wettability

Wetting describes a process of a droplet wetting and spreading on a certain solid surface along with the new solid–liquid interface formation and the original solid–gas interface fading away [5, 68, 69]. Figure 4 illustrates a wetting equilibrium state of molten solder spreading on Cu substrate, where four parameters including θ, γ_{gs}, γ_{ls} and γ_{gl} represent contact angle, surface tension of solid/gas interface, solid/liquid interface and gas/liquid interface, respectively. At this moment, they follow the classical Young's equation shown below [70]:

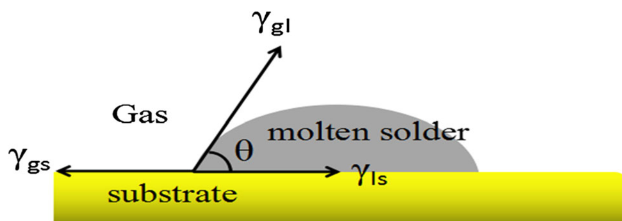

Fig. 4 Schematic drawing of wetting process of molten solder on the substrate

$$\cos\theta = \frac{\gamma_{gs} - \gamma_{ls}}{\gamma_{gl}} \quad (1)$$

Generally, the contact angle θ in Eq. (1) indicates the wettability, which can also be evaluated by indexes of spreading area, wetting time and wetting force [71]. In order to obtain a reliable solder joint with satisfactory wettability, the contact angle θ is longingly expected to be minimized to a certain extent for too small θ might lead to bridging defects [6, 60]. It should be noted Sn–Ag–Cu solders generally performed inferior wettability to eutectic Sn–Pb solder, indicative of an urgent demand for wettability enhancement [8]. The most common and effective methodology to realize it is known to add foreign elements into Sn–Ag–Cu solders. Besides, factors like soldering temperature adjustment, flux or substrate types can more or less influence the wettability of Sn–Ag–Cu solders [10, 72].

As is well known, surface-active RE addition with appropriate content has been attached much more importance than other additives addition (e.g., Ni [63], P [64], In [73], Bi [74], Fe_2O_3 [12], Al_2O_3 [35], TiO_2 [75]), as displayed in Table 2. Clearly, RE addition makes a distinct improvement in wettability of corresponding Sn–Ag–Cu solder. For instance, the influence of Eu addition (x = 0–0.5 wt%) on wetting behaviors of Sn–Ag–Cu solder in air and N_2 atmospheres through wetting balance test was illustrated in Fig. 5 [22]. Apparently, Sn–Ag–Cu–xEu solders in N_2 atmosphere overall performs superior wettability to those examined in air due to much more severe oxidation of solders in air than that in N_2 atmosphere. It should be noted the optimum content of Eu addition is irrelevant to atmosphere type since it was examined to be 0.04 wt% whether in air or in N_2. This enhancement in wettability is due to a decrement in γ_{gl} in Eq. (1) contributed by the segregation of surface-active Eu on molten solder surface. However, a further Eu addition beyond 0.04 wt% provides no more improvement in wettability due to the bulk Sn–Eu phase oxidation that can worsen liquid solder fluxility. Therefore, the content of Eu addition into Sn–Ag–Cu solder is demanded to be strictly managed in an optimal range for prime wettability. Similarly, for Sn–Ag–Cu solder with other RE addition like Nd (0–0.5 wt%) [3], Yb (0–0.5 wt%) [60] and Pr (0–0.5 wt%) [25], the hard and brittle Sn–RE oxidation phases might also present when their addition content is beyond the fittest concentration (∼0.05 wt%). In addition, alloys of Bi and In addition with appropriate content also play a relative positive role in wettability improvement. For example, elemental Bi with intrinsically low surface tension ($\sigma_{Sn} = 0.55$ N/m, $\sigma_{Ag} = 0.03$ N/m, $\sigma_{Cu} = 1.35$ N/m, $\sigma_{Bi} = 0.39$ N/m) has the capacity to decrease the surface tension of Sn–3.5Ag–0.5Cu solder. Hence, solder with Bi addition is more ready to wet and spread over the copper

Table 2 Results of wettablility evaluations from relative literatures

Sn–Ag–Cu based solders	Test range x/wt %	The most optimum content c/wt %	Temperature T/°C	Sustrate	Flux	Evaluations at the most suitable content
SAC0307-xP [64]	0.004	A little decrease	260	Cu	WF-6400	Spreading area:47.3 mm^2
SAC0507-xGa [5]	0–1	0.5	245/255/265/275	Cu	Water-soluble	–
SAC125-xIn [73]	0–0.8	0.4–0.6	230/240/250	Cu	Water-soluble WF6063 M	–
SAC305-xP/xNi [63]	0.01/0.1	Improvement/A little increase	260	Cu	$ZnCl_2$ (22 wt%) + NH_4Cl (2 wt%) + deionized water (76 wt%)	Wetting time:0.358 s/0.488 s
SAC355-xBi [74]	0–1.5	0.5	240	Cu	ROLl A	Wetting time:1.07 s
SAC-xEu [22]	0–0.5	0.04	245	Cu	–	–
SAC-xYb [60]	0–0.5	0.05	–	Cu	–	–
SAC387-xNd [3]	0–0.5	0.05	240/250/260	Cu	Rosin mildly activated (RMA)	–
SAC387-xPr [25]	0–0.5	0.05	260	Cu	RMA	Spreading area: 63.27 mm^2
SAC107-xFe_2O_3 [12]	0–1.0	0.4	260	Cu	–	Wetting time:1.10 s
SAC305-xTiO_2 [75]	0–0.75	0.25	270	Cu	RMA	–
SAC305-xAl_2O_3 [35]	0–1	0.5	250	Cu	–	Contact angle:28.9°
SAC355-x$BaTiO_3$ [77]	0–0.4	0.2	–	Cu	–	Spreading coefficient: 0.7836

"_" represent no recorded data, respectively. SAC0307, SAC0507, SAC107, SAC125, SAC305, SAC355, SAC387 and SAC397 stand for Sn–0.3Ag–0.7Cu, Sn–0.5Ag–0.7Cu, Sn–1.0Ag–0.7Cu, Sn–1.2Ag–0.5Cu, Sn–3.0Ag–0.5Cu, Sn–3.5Ag–0.5Cu, Sn–3.8Ag–0.7Cu, and Sn–3.9Ag–0.7Cu, respectively

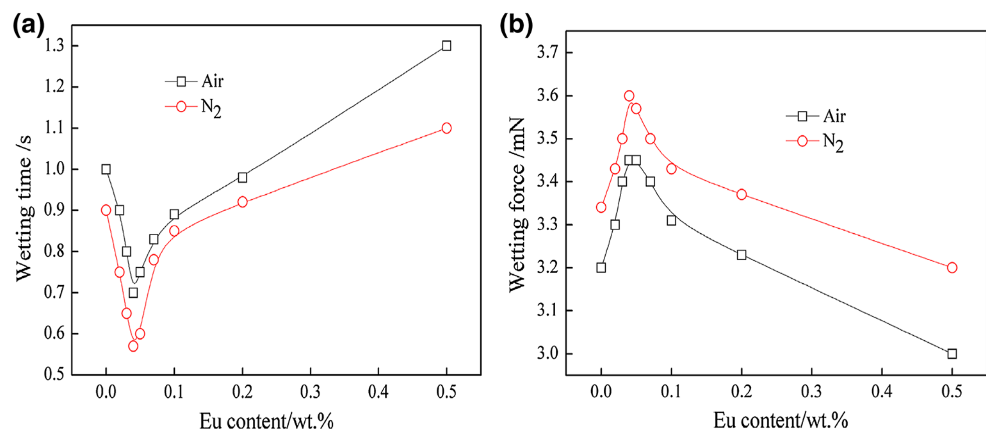

Fig. 5 Wetting behavior of SnAgCu–xEu solders: **a** wetting time, **b** wetting force [22]

wire in comparison to its monolithic counterpart [74]. Different from RE or Bi addition, as In-containing Sn–0.7Ag–0.5Cu solders wet and spread on Cu substrate, elemental In is prone to combine with elemental Cu (mainly from Cu substrate) to form Cu–In IMCs (based on Cu–In phase diagram [76]). This contributes to a visible reduction in γ_{ls} instead of that in γ_{gl} in Eq. (1), thus decreasing the contact angle θ [73]. Furthermore, due to the unique adsorption effect that nanoparticles (e.g., TiO_2 [75], Al_2O_3 [35], Fe_2O_3 [12], $BaTiO_3$ [77]) own, they are inclined to be adsorbed on a solid surface (Cu coupon in the wetting balance test). So, the surface tension of Sn–Ag–Cu molten solder (γ_{gl}) could be lowered with these nanoparticles incorporation, indicative of a satisfactory

wetting performance. Worthy of note is that the wetting performance is sensitive to nanoparticles content for excessive nanoparticles will agglomerate with each other and then float on the surface of molten solder which can impede the wetting process [75].

For a given type of solder using certain flux, the wettability could also be distinctly enhanced as the soldering temperature elevated moderately. For example, an overall improved wettability of Sn–3.8Ag–0.7Cu–xNd (x = 0–0.5 wt%) solders using rosin mildly activated (RMA) flux could be realized with a raised temperature from 240 to 260 °C [3]. In addition, with the examined temperature elevating from 245 to 275 °C, the wettability of Sn–0.5Ag–0.7Cu–0.5 Ga solder was gradually improved with the help of water-soluble (WS) flux due to the accelerated atom diffusion that occurred at the interface [5]. It's worth mentioning that the surface-active Ga is liable to aggregate on the liquid solder surface, so that it can decrease γ_{gl} in Eq. (1) and eventually lower the contact angle θ.

Flux is known to serve as a crucial role in eliminating the surface oxides of molten solder and substrate, creating conditions for molten solder to fill and spread over substrate, protecting liquid solder from oxidation, making the interfacial reaction more active, etc. So, a novel flux matching with a suitable metallic substrate is also significantly critical to be conducive to the wetting process. For instance, Ref. [78] reported that Sn–2.8Ag–0.5Cu–1.0Bi solder was wetable on either Cu or Ni substrate and this process was highly dependent on the flux type. To be more specific, NC flux fitted Cu substrate, while WS flux with high activity was suitable for Ni substrate and non-wetting occurred for Ni substrate if R flux was utilized. In addition, with the assistance of novel flux containing 22 wt% $ZnCl_2$, 2 wt% NH_4Cl and 76 wt% deionized water, the wettability of Sn–3.0Ag–0.5Cu–0.01P solder at 260 °C was strengthened [63]. To date, flux for Sn–Zn solders have been applied for a patent by our group, while that exclusively for Sn–Ag–Cu solders haven't been researched which can become the future focus for wettability improvement.

5 Microstructures

As is well known, it is the solder microstructure that greatly determines the mechanical properties as well as in-service performance of solder. According to the Sn–Ag–Cu ternary phase diagram (Fig. 6 [79]), the microstructure of air-cooled Sn–Ag–Cu eutectic solder mainly consists of primary β-Sn dendrites, ternary eutectic structure (scallop-type Cu_6Sn_5 + plate-like Ag_3Sn) and other bulk IMCs. It was found large plate-like Ag_3Sn growth in the solder matrix may cause strain localization at the boundary of β-Sn phase with the potential risk of preferred crack growth at the interface. Consequently, the mechanical properties of solder joint were degraded with the fatigue life shortened. However, this issue of bulk Ag_3Sn growth in the solder matrix can be relieved by means of either raising the cooling rate or lowering the silver content in Sn–Ag–Cu solders [80, 81]. For instance, as the reflowed solders were cooled under the conditions of water, air, and furnace, the Ag_3Sn in the solder matrix would emerge with particle-shape, branch-shape and plate-shape, respectively [82]. Besides, the method of micro-alloying was also confirmed to be effective into produce a refined and stabilized microstructure with much finer IMCs uniformly distributed.

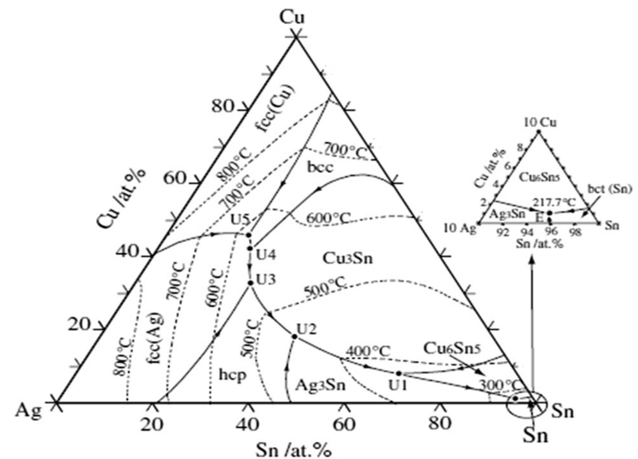

Fig. 6 Sn–Ag–Cu ternary phase diagram [79]

As is well-known, a notable effect of RE addition on solder alloys is microstructure refinement [3, 25, 71, 83]. Figure 7 shows the schematic diagrams of how RE addition influences IMC growth. When added extremely little into Sn–Ag–Cu solders, elemental RE is prone to distribute at the interfaces of IMCs for its surface-active quality, forming a diffusion barrier to Sn–Ag and Sn–Cu diffusion (Fig. 7a). When RE is added with optimal content, it will combine with elemental Sn to form fine Sn–RE particles for its higher affinity for elemental Sn, as listed in Table 3. So, the solidification process can be accelerated and the formation of extremely large IMCs will be impeded (seeing Fig. 7b). As RE addition constantly increases, Sn–RE particles grow up along with their oxidation, thus causing the occurrence of reliability issue of Sn whisker (seeing Fig. 7b, c), which will be detailedly introduced in Sect. 11. For instance, the influence of Yb addition on microstructure evolution of nominally air-cooled Sn–Ag–Cu–xYb (x = 0, 0.05, 0.1 wt%) ternary alloys was shown in Fig. 8 [60]. As can be seen from Fig. 8a, the microstructure of original SnAgCu ternary alloy consists of gray tilt primary-Sn dendrites surrounded by the Ag_3Sn, Cu_6Sn_5 and β-Sn

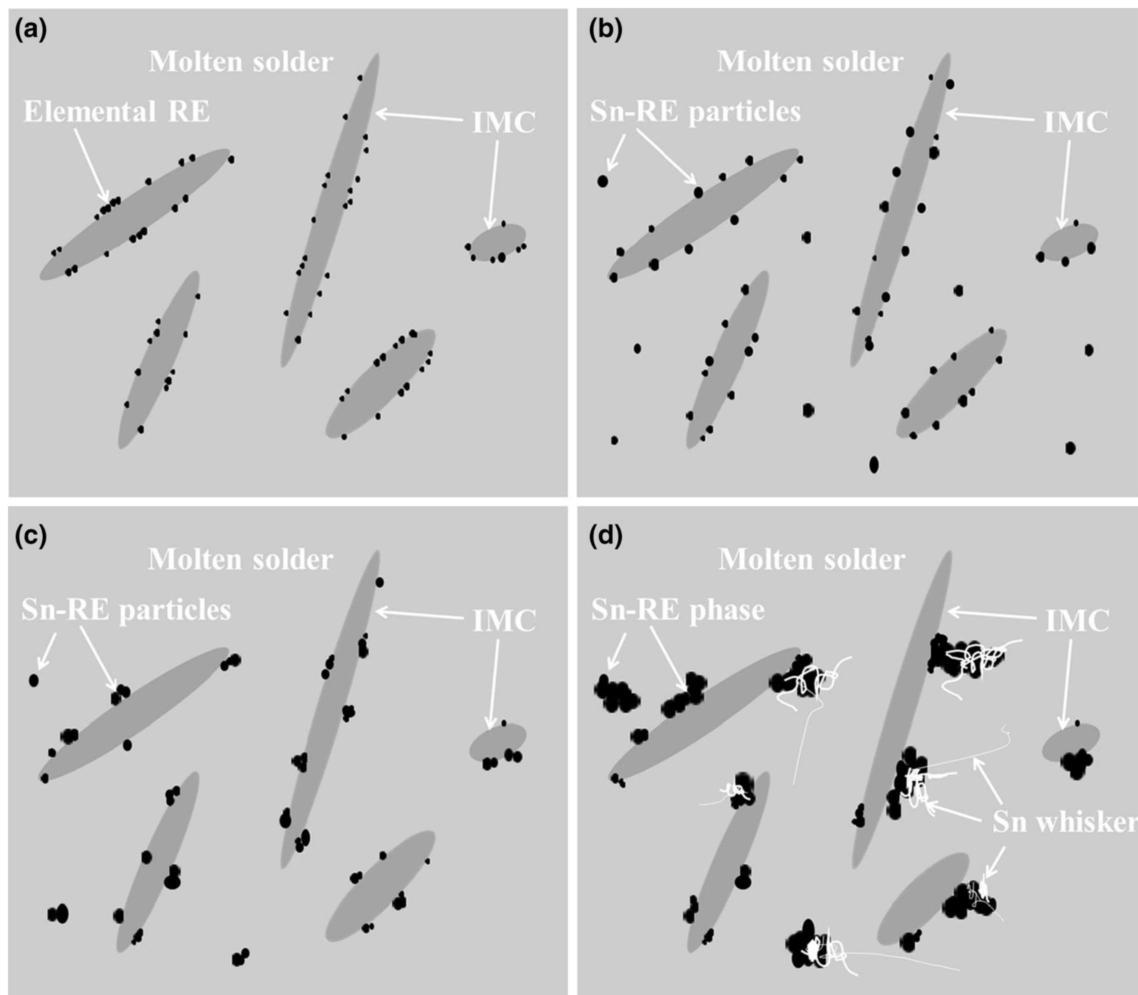

Fig. 7 Schematic diagrams of how RE content influences intermetallic compounds (IMCs) growth: **a** extremely little RE addition, **b** optimal RE addition (∼0.05 wt%), **c** RE content little over the optimal (0.05–0.1 wt%), **d** excessive RE addition (>0.1 wt%)

Table 3 Thermodynamic parameters of element affinity between Pr and Sn, Cu, and Ag [83]

Binary system	Z/r_kA	Z/r_kB	Z/r_kA Z/r_kB	X_A	X_B	ΔX	η
Sn–Pr	5.64	2.68	2.10	1.8	1.2	0.6	2.7
Pr–Cu	2.68	1.04	2.58	1.2	1.9	−0.7	1.88
Pr–Ag	2.68	0.79	2.98	1.2	1.9	−0.7	2.88
Sn–Nd	5.64	2.73	2.10	1.8	1.14	0.6	2.73
Nd–Cu	2.73	1.04	2.58	1.14	1.9	−0.7	2.70
Nd–Ag	2.73	0.79	2.98	1.14	1.9	−0.7	1.87

η means chemical affinity parameter, indicating the chemical affinity between element A and element B (The larger the values of the thermodynamic parameters, the stronger the interaction will be). Additionally, ΔX represents difference in electronegativity between A and B

eutectic network. With 0.05 wt% Yb addition, both sizes of β-Sn dendrite and eutectic structure were distinctly decreased to become finer particles (Fig. 8b). However, a further Yb addition to 0.1 wt% not only coarsened the microstructure, but also caused the emergence of hard and brittle phases that were detrimental to the tensile strength. Analysis by SEM/EDS indicated that this phase contained elemental Sn and Yb, with an atomic ratio of approximately 3:1. It were finally identified to be $YbSn_3$ compound with the help of Sn–Yb alloy phase diagram. Likewise, a SEM image comparison between air-cooled Sn–Ag–Cu and Sn–Ag–Cu–0.04Eu solders was also made.

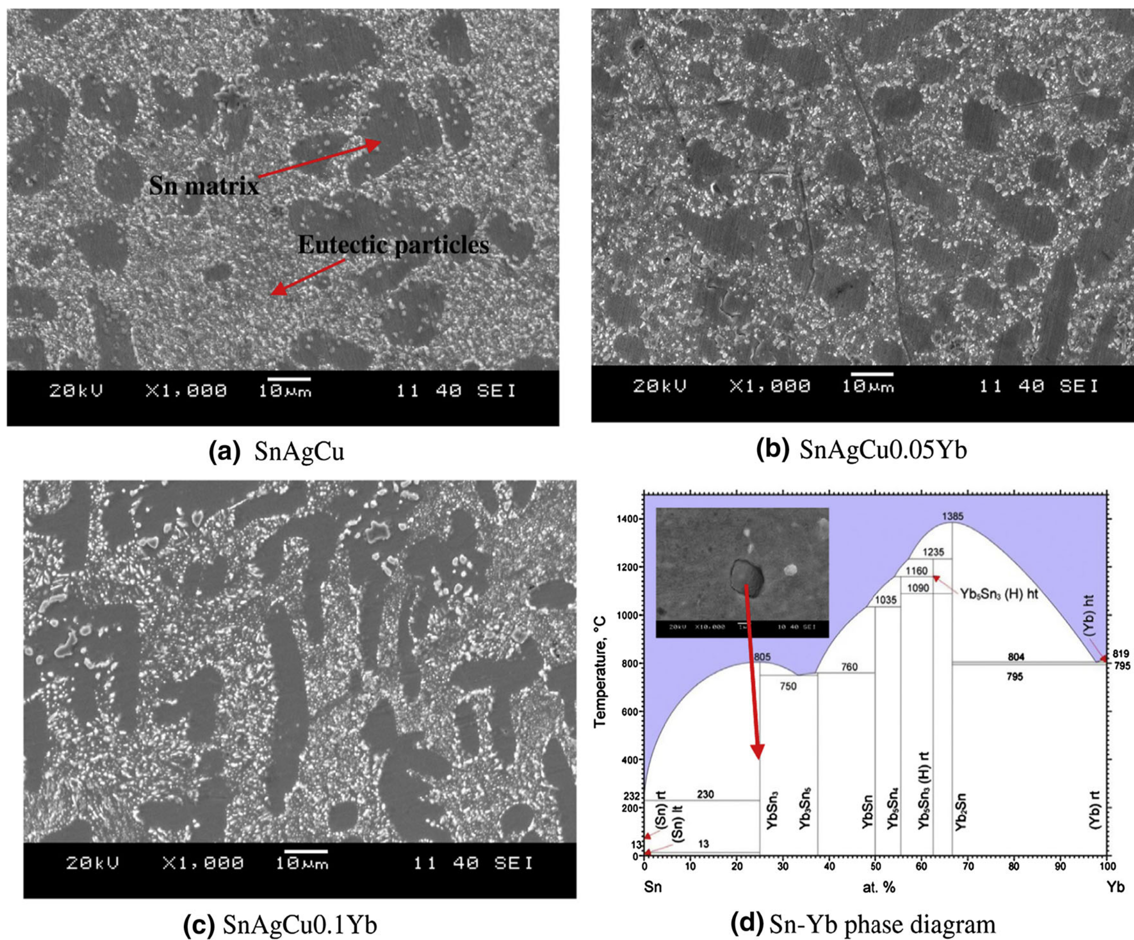

Fig. 8 SEM micrographs of nominally air-cooled Sn–Ag–Cu–xYb (x = 0, 0.05, 0.1 wt%) ternary alloys [60]

The results showed that Sn–Ag–Cu–0.04Eu solder displayed a much finer microstructure with more uniform and smaller eutectic particles (Cu_6Sn_5 and Ag_3Sn) dispersed within it when compared with its plain counterpart [22].

Besides, other alloys addition with appropriate content (e.g., Fe, Co, Ni, Bi, Zn, Ti) also plays a significant role in ameliorating the microstructure of Sn–Ag–Cu solders, as summarized in Table 4. It is reasonable to conclude that the microstructure modification is generally associated with the formation of solid solutions (e.g., $(Cu,Ni)_6Sn_5$, $(Co_xCu_{1-x})_6Sn_5$ and $(Ni_xCu_{1-x})_6Sn_5$) or tiny particles like $(Cu,Ag)_5Zn_8$ and Ti_2Sn_3 which can provide a great deal of additional nucleation sites for relative IMC phase crystallization. Then, the solidification process can be accelerated, so that it leaves inadequate time for IMC phase growth. Consequently, the microstructure of Sn–Ag–Cu solder free of large IMCs is beneficial to the mechanical properties of solders. For example, adding Fe into Sn–1Ag–0.5Cu solder not only makes the large Ag_3Sn in solder matrix disappear but also retains the mechanical properties during high temperature aging process. Worthy of note is the phenomenon of fractional substitution of Fe into the Ag_3Sn IMC particles in the place of Ag atom, which is verified by the EDX analysis, TEM observations (Fig. 9 [84]) and the criteria to classify the solid solubility of fifty alloy systems (DG method) [85] (atomic size difference between Ag and Fe: <13 %; electronegativity difference: −0.1 on the Pauling scale). On the one hand, this partial replacement of Ag atom in Ag_3Sn by Fe atom generates the lattice strain in the Ag_3Sn. So the diffusion rate of Ag atoms is reduced in the Sn matrix upon aging, which can slow down the microstructure coarsening rate. On the other hand, Fe solute atoms in the Sn matrix are capable to block Ag atoms moving from the Sn matrix surrounded by smaller Ag_3Sn particles towards that surrounded by larger Ag_3Sn particles. Thus, the Ag atoms supply required for continuous growth of small Ag_3Sn is gradually cut down. Similarly, due to the similar atomic radius as Cu, (r_{Cu}: 0.128 nm; r_{Ni}:0.125 nm; r_{Co}: 0.125 nm), the elemental Co (0.05 wt%) and Ni (0.05 wt%) was observed to be concentrated in $(Co_xCu_{1-x})_6Sn_5$ and $(Ni_xCu_{1-x})_6Sn_5$ IMCs, respectively [86]. These Ni- or Co- containing IMCs

Table 4 The effects of relative alloy elements on the microstructures of Sn–Ag–Cu solder alloys

Sn–Ag–Cu based solders	Changes of Sn martrix	Changes of IMCs
Sn–0.5Ag–0.7Cu–0.5 Ga [5]	Refined	IMCs become smaller and more uniformly distributed in the matrix; black phases, harmful to the mechanical properties, appear with the composition of Sn, Cu and Ga as Ga reaches 0.5 wt%
Sn–0.5Ag–0.7Cu–0.05Ni [7]	Refined	Stable $(Cu,Ni)_6Sn_5$ was formed; The volume fraction of the IMCs increases
Sn–1.0Ag–0.5Cu–0.06Ni [56]	Refined with their volume fraction decreased	New Ni_3Sn_4 IMCs appear; The fiber-like IMCs are coarsened while dot-shaped precipitates are finer
Sn–1.0Ag–0.3Cu–xZn (x = 0–3 wt%) [88]	The formations of dendritic β-Sn phase decrease	More uniformly-distributed; New plate-like $(Cu, Ag)_5Zn_8$ IMCs appear; Needle-like Ag_3Sn and polygon Cu_6Sn_5 particles decrease
Sn–1.0Ag–0.5Cu–0.5Sb [56]	The volume fraction of the primary β-Sn phase decreases	Minor amount of Sb dissolves in the Sn matrix due to its relatively similar radius to Sn atom; The eutectic area increases (more refined IMCs of Cu_6Sn_5 and Ag_3Sn in size)
Sn–3.5Ag–0.5Cu–xTi (x = 0–1 wt%) [44]	Refined	New Ti_2Sn_3 IMCs appear; The eutectic area (β-Sn + Ag_3Sn IMCs) becomes more refined
Sn–1Ag–0.5Cu–xFe (x = 0–0.3 wt%) [45]	Enlarged	Large $FeSn_2$ IMCs besides small Ag_3Sn and Cu_6Sn_5 IMCs are formed located at the eutectic regions

"/" represent space character

formed in the Sn–0.1Ag–0.7Cu solder matrix with a cooling rate around 5 °C/s provided more nucleation sites for β-Sn growth, so that inadequate time was left for β-Sn growth. As a result, a more uniform microstructure with smaller β-Sn dendrites could be obtained. Besides, according to micro-observation of coarser $(Co_xCu_{1-x})_6Sn_5$ than $(Ni_xCu_{1-x})_6Sn_5$ in the matrix, elemental Ni was capable to better refine IMCs in size than elemental Co. Additionally, the microstructure development of as-solidified Sn–1.5Ag–0.7Cu–xBi (x = 0, 1, 3 wt%) with a cooling rate of 6–8 °C/s was also investigated by El-Daly [87]. The results revealed that the microstructure of 1 wt% Bi-containing solder is comprised of more notable primary β-Sn grains in comparison to that of the plain solder. Besides, the size of needle-like Ag_3Sn (light gray) and Cu_6Sn_5 (dark gray) ranged from 5.0 to 20.0 and from 0.5 to 5.0 μm, respectively. Also, the microstructure of Sn–1.5Ag–0.7Cu–1Bi solder was free of any precipitated Bi particles due to large solubility of Bi in Sn (about 1.0–1.8 wt% at room temperature). However, a further Bi addition to 3.0 wt% resulted in the emergence of white clusters of Bi precipitates uniformly distributed within the solder matrix that played a dominant role in creep deformation. Moreover, the effects of Zn addition [88] on microstructure evolution of Sn–2.0Ag–0.7Cu with a cooling rate of 6–8 °C/s were studied by FE-SEM equipped with EDS analysis. The results suggested a minor Zn addition (1.5 wt%) into Sn–2.0Ag–0.7Cu solder didn't altered the distribution of needle-like Ag_3Sn (10.0–80.0 μm), Cu_6Sn_5 (polygon shape, 5.0–9.0 μm) and β-Sn grains in the original matrix. However, due to the high interfacial energy between solid solder and IMC particles, this distribution might lead to untimely failure. Fortunately, the existence of $\gamma-(Cu,Ag)_5Zn_8$ IMCs can significantly retard the growth rate of Ag_3Sn and Cu_6Sn_5, whose formation relies on both Ag and Zn concentration. Also, since $(Cu,Ag)_5Zn_8$ is more stable than other IMCs (Cu_6Sn_5, Ag_3Sn) in the solder matrix, it become more difficult for the occurrence of crack propagation in $(Cu,Ag)_5Zn_8$ precipitates. Furthermore, Fig. 10 [44] displayed the SEM micrographs of as-solidified Sn–3.5Ag–0.5Cu solder alloying with Ti (0–1 wt%). Clearly, the microstructure of Sn–3.5Ag–0.5Cu solder exhibited apparent light regions of coarse β-Sn grains (24.8 ± 5.9 μm) and dark eutectic regions of β-Sn and Ag_3Sn (6.8 ± 2.8 μm). As Ti addition rises up to 1 wt%, the microstructure of the solder is remarkably refined with

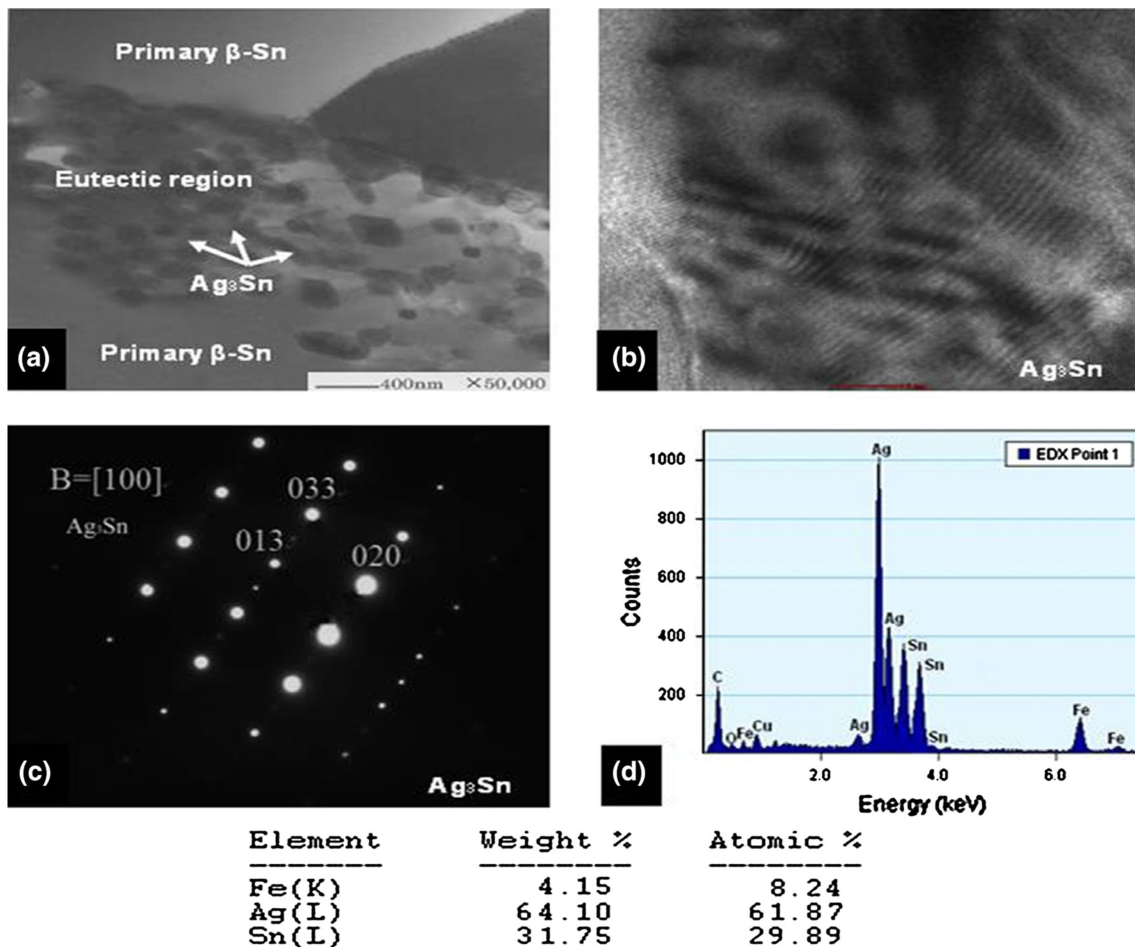

Element	Weight %	Atomic %
Fe(K)	4.15	8.24
Ag(L)	64.10	61.87
Sn(L)	31.75	29.89

Fig. 9 TEM analysis of the Ag_3Sn particles formed at the eutectic region in the as-cast Fe-modified solder: **a** TEM image, **b** high resolution TEM image, **c** micro-electron-beam diffraction pattern, and **d** TEM-EDX spectrum [84]

the average grain size and the eutectic area width approaching to the minimum value of 4.8 ± 1.7 and 1.2 ± 0.4 μm, respectively. This refinement is highly associated with the favorable mechanical production—heterogeneous Ti–Sn IMC, which is identified as Ti_2Sn_3 phase (Fig. 10d) by EDS detection due to its lower standard Gibbs free energy than that for other possible IMCs, including Ag–Sn, Cu–Sn, Ti–Cu and Ti–Ag.

Recently, refractory nanoparticles with moderate addition quantity into solders also have been demonstrated as an effective and affordable approach to refine microstructures because of their adsorption effect which may cause a pinning effect on IMC growth. For instance, surface-active TiO_2 nanoparticles with suitable addition content [75] are inclined to be adsorbed on the surface of primary precipitated IMC or β-Sn grains to lower the surface energy. So they can form diffusion barriers to Sn–Ag or Sn–Cu diffusion and effectively impede the IMC growth (Ag_3Sn and Cu_6Sn_5) during the melting sequence. Also, the introduction of 0.07 wt% GNSs into Sn–3Ag–0.5Cu solder decreased the size of relevant IMCs (from ∼1.96 to ∼1.21 μm) due to more nucleation sites for IMCs growth provided by restacked GNSs embedded in the pitting on the β-Sn surface of the solder, as validated in Fig. 11 [48]. As IMC grains grew and encountered the surface of GNSs, the incremental interfacial energy between the IMCs and GNSs caused an increase in the thermodynamic resistance of IMC grain growth. Consequently, the relative metal atom diffusion as well as the IMC growth could be effectively inhibited. Worthy of note is that if nanoparticles are excessively introduced, they will get entangled with each other driven by van der Waals forces, thus in reverse weakening the depression effect on IMCs growth exerted by nanoparticles addition. Therefore, much importance should be attached to the content of nanoparticles addition for the maximized refinement of IMCs in size. Moreover, nanoparticles also provided additional sites for β-Sn growth which can

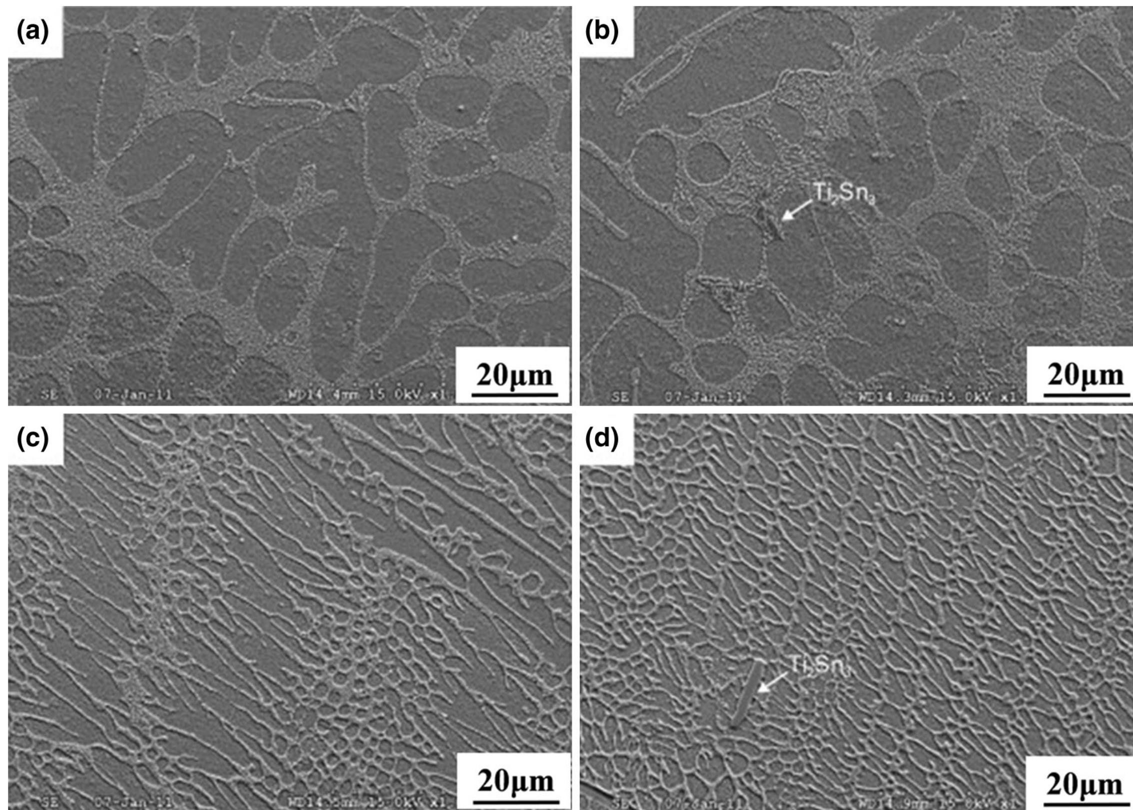

Fig. 10 SEM micrograph of the lead-free Sn–3.5Ag–0.5Cu–xTi solders. **a** Sn–3.5Ag–0.5Cu, **b** Sn–3.5Ag–0.5Cu–0.25Ti, **c** Sn–3.5Ag–0.5Cu–0.5Ti, **d** Sn–3.5Ag–0.5Cu–1Ti [44]

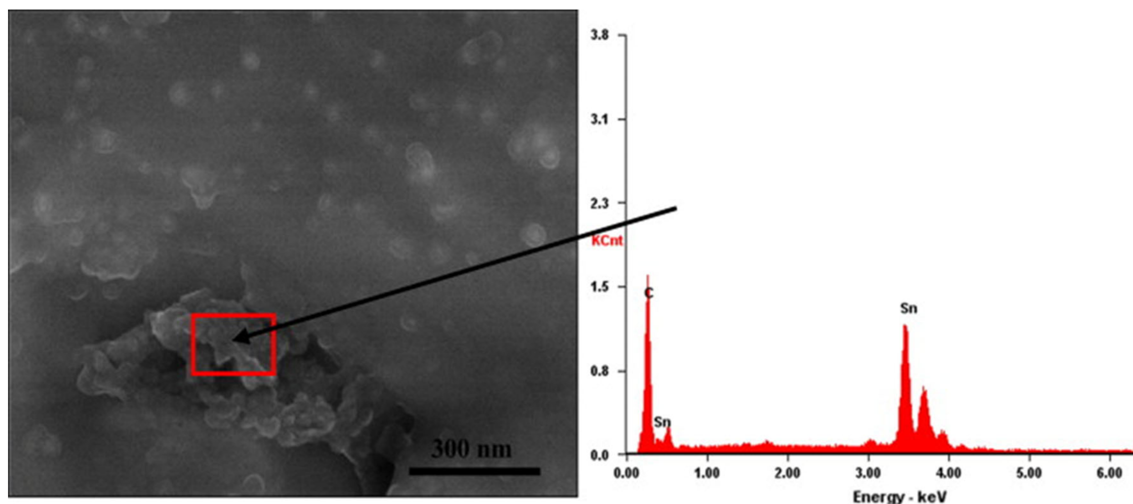

Fig. 11 Representative SEM image of restacking GNSs in the pitting with corresponding EDX spectrum [48]

stimulate the solidification process and impede the excessive growth of β-Sn phases. This was verified by the evidence of primary β-Sn phase initially nucleating adherent to the surface of $BaTiO_3$ particles [77] or FeCo magnetic nanoparticles (MNPs) [89] in the solder matrix of $BaTiO_3$-containing Sn–1.0Ag–0.5Cu and Sn–Ag–Cu solder containing FeCo MNPs.

6 Interfacial reactions

During soldering process, interfacial reaction occurs accompanying with interfacial IMCs nucleating and gradually developing to a layer between molten solder and a certain metallic substrate [4, 9]. Actually, this reaction process includes two diffusion procedures: molten state

diffusion and solid state diffusion, which are devided based on the diffusion rate and affected by temperature. In the initial reaction period, the temperature of molten solder reaches approximately 250 °C which gradually decreases down to 100–150 °C as the molten solder slowly solidifies, just similar to employing aging treatments to solders [1, 10, 39]. The marker displacement validated that elemental Cu is the dominant species to form Cu_6Sn_5 at the interface of solder/Cu substrate, indicating that Cu–Sn IMCs are formed by transporting Cu atoms across the Cu_6Sn_5 IMC, which takes place at the Cu_6Sn_5/Sn interface [90, 91]. Considering the inherent hard and brittle nature of Cu_6Sn_5 IMCs, interfacial IMC layer with certain thickness at the solder/substrate interface become substantially important for its determination in the reliability of solder joint [13, 34, 41]. To date, many attempts have been made to limit the excessive growth of interfacial IMC layer and the most successful one is micro-alloying, as indicated in Table 5. In this section, the knowledge of solder/substrate interfacial structure evolution and crucial mechanisms in them from the viewpoint of metallurgy will be introduced to fully understand reliability issues and better optimize the soldering process.

A considerable amount of research has confirmed the contribution to impeding the interfacial IMC growth that RE does (e.g., Pr [25], Nd [3], Ce [92], Yb [60]). The surface-active RE elements are inclined to react with elemental Sn (pro-Sn characteristic), so that the activity of elemental Sn at the interface of Cu_6Sn_5/solder is lowered by forming Sn–RE compounds. As a result, the driving force to form Cu–Sn or Ag–Sn IMCs is depressed that finally contributes to the decrease in the thickness of interfacial IMC layer. For example, the 0.05 wt% Yb-doped solder/Cu interface appears with relatively flat morphology and smaller thickness than that at the Sn–Ag–Cu/Cu interface, as illustrated in Fig. 12a, c. After deep etching (Fig. 12b, d), the Cu_6Sn_5 grains of Sn–Ag–Cu–Yb solder joint exhibited an obviously smaller size than those of the plain solder joints. Additionally, alloying 0.05 wt% Pr or 0.05 wt% Nd into Sn–3.8Ag–0.7Cu solder were also confirmed to substantially slow down the growth rate of scallop-type Cu_6Sn_5 IMCs located at composite solder/Cu interface. However, excessive addition of Pr and Nd to 1 wt% resulted in the emergence of hard and brittle $PrSn_3$ and $NdSn_3$ IMC particles on top surface of the Cu_6Sn_5 IMC layer, which were definitely detrimental to the mechanical properties despite with the capacity to interrupt interfacial Cu_6Sn_5 IMCs growth. Our group now contributes to investigating the influence of RE addition on the (interfacial) microstructures of low-Ag Sn–Ag–Cu solders which is a future application trend when considering production cost.

Refractory nanoparticles addition with moderate content (e.g., Mo [34], Al_2O_3 [93], TiO_2 [75], $SrTiO_3$ [94], Y_2O_3 [28]) can also significantly hinder the growth of interfacial IMC layer. This is mainly because that they have strong tendency to be adsorbed on the surface of interfacial Cu_6Sn_5, thus exerting a pinning effect on the growth of interfacial Cu_6Sn_5. Figure 13 [34] shows the schematic diagram of how Mo nanoparticles affect Cu_6Sn_5 scallop growth. As can be seen, Mo nanoparticles with high T_m and low reactivity, are mainly adsorbed at the growth front of IMC scallops which can block the channels between IMC scallops. So, it causes a decrement in interfacial reaction flux

Table 5 The effects of alloys and nanoparticles on thinning IMC layers of Sn–Ag–Cu solders

Sn–Ag–Cu based solders	Levels of thickness decrease in IMC layer influenced by alloys and nanoparticles
Sn–0.5Ag–0.7Cu–Ga [39]	When the content of Ga addition reaches 0.5 wt%, the average thickness of IMC layer approaches to 3.59 µm, about 58.9 % thinner than that of its plain solder
Sn–3.0Ag–0.5Cu–Pd [96]	The ratio of Cu_3Sn IMC thickness to the total IMC thickness was remarkably decreased from ~0.42 to ~0.3 µm with 0.1 wt% Pd addition
Sn–3.8Ag–0.7Cu–RE(Nd [3], Pr [25])	With the addition of 0.05 wt% Nd or 0.05 wt% Pr to the solder, the average IMC layer thickness at composite solder/Cu interface gives a decrease of 45.8 and 31 %, respectively compared to that at plain solder/Cu interface
Sn–3.8Ag–0.7Cu–nMo [34]	0.1 wt% Mo nanoparticles addition suppresses the interfacial IMC thickness from 1.5 to 0.95 µm, and meanwhile reduces the scallop diameter from 2.2 to 1.3 µm
Sn–3.0Ag–0.5Cu–TiO_2 [75]	With the concentration of TiO_2 addition increasing from 0 to 0.1 wt and to 0.25 wt%, the interfacial IMC layer thickness of Sn–3.0Ag–0.5Cu solders is rapidly reduced from 7.9 to 4.2 and to 3.5 µm, respectively
Sn–3.0Ag–0.5Cu–$SrTiO_3$ [94]	After one reflow cycle, adding 0.5 wt% $SrTiO_3$ nanoparticles depresses the IMC layer thickness of the solder from 2.1 to 1.7 µm
Sn–Ag–Cu–n(Ni–CNT) [122]	The addition of Ni–CNTs decreases the thickness of interfacial IMC layer from 2.30 to 1.82 µm under the as-soldered condition

"n" stands for nanoparticles

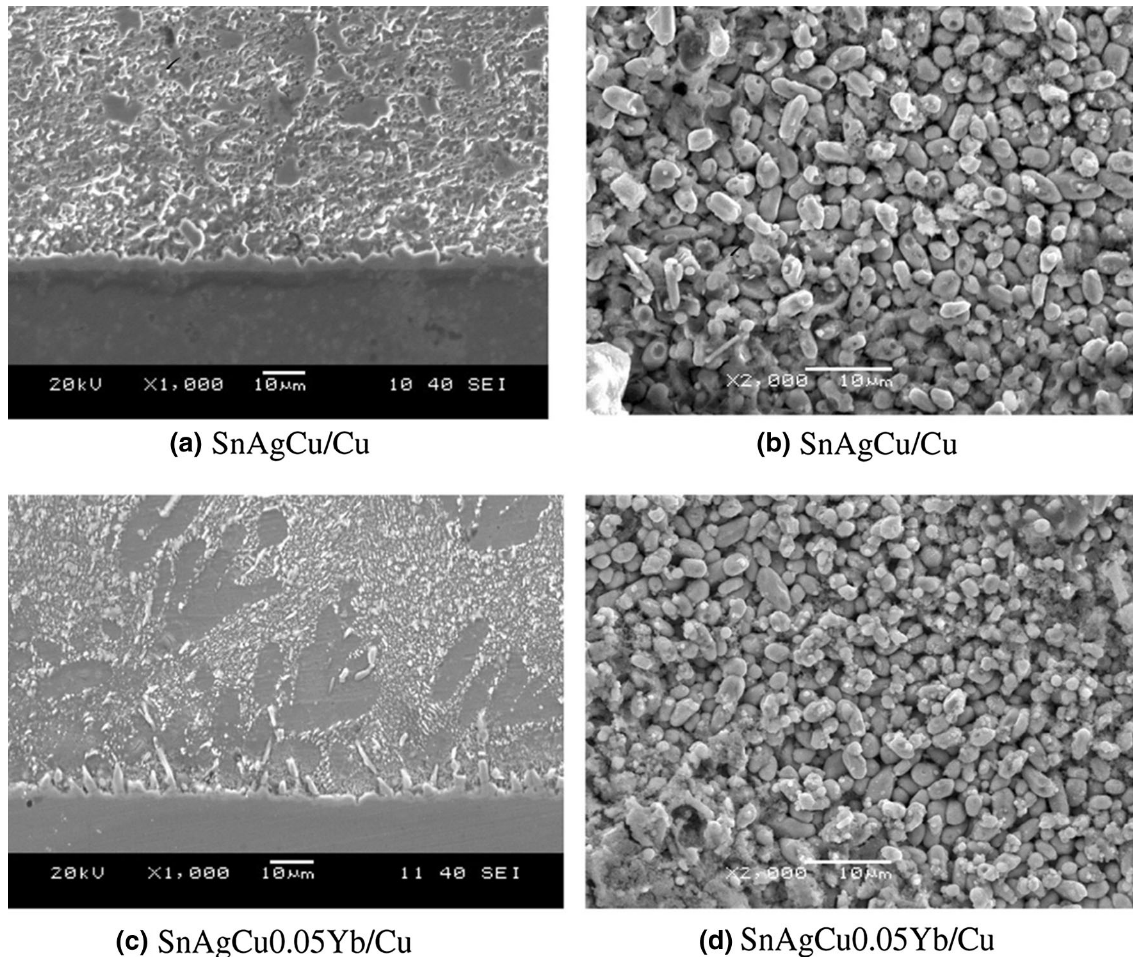

(a) SnAgCu/Cu **(b)** SnAgCu/Cu **(c)** SnAgCu0.05Yb/Cu **(d)** SnAgCu0.05Yb/Cu

Fig. 12 Morphologies of as-soldered microstructure of the interfacial IMC layers in plain and Yb-doped solder samples [60]

(J^I), indicative of a suppressive effect on Cu atoms movement from substrate towards liquid solder. Besides, a decline in ripening flux (J^R) is obtained as well since Mo nanoparticles adhered on the IMC surface act as barriers to the coalescence of neighboring scallops, leading to a decrement in scallop diameter. Different from the adsorption behavior of Mo nanoparticles, TiO_2 nanoparticles have more tendency to be adsorbed on the surface of Cu substrate, as illustrated in Fig. 14 [75]. So, effective diffusion barriers to Cu–Sn diffusion involved in interfacial reaction are formed, which eventually thins the interfacial IMC layers during reflow operation. However, an excessive TiO_2 addition (0.5 and 0.75 wt%) tend to agglomerate with each other to minimize the surface free energy, thus greatly weakening the adsorption effect on Cu substrate. Consequently, the suppressive effect on relative interfacial IMC growth significantly debased, as indicated in Fig. 14b. Hence, the content of these surface-active nanoparticles addition is required to be strictly controlled to maximize their obstructive role in interfacial IMC growth.

Solid interfacial reaction occurs during isothermal aging which is a commonly-applied treatment to evaluate the effects of alloying on service properties of solder joint. It was once stated in Ref. [95] that there are no energetic way that additives could influence the driving forces for Sn and Cu diffusion through the Cu–Sn IMCs in solid interfacial reactions except they alter the stability of IMCs via dissolving in them or changing the activity of Sn through moving into the solid Sn. For example, research on the interfacial morphology evolution of Sn–3Ag–0.5Cu–xPd (x = 0.1–0.7 wt%)/Cu solder joint revealed that trace quantity of Pd (1.7–2.2 at %) was dissolved in the Cu_6Sn_5 IMC layer but no meaningful content of Pd was incorporated into the Cu_3Sn during isothermal aging at 180 °C, over all aging times. As the content of Pd increased beyond 0.5 wt%, a mount of isolated domains, confirmed to be solid solution $(Pd,Cu)Sn_4$, emerged at the composite solder/Cu interface. This solid solution ($(Pd,Cu)Sn_4$) enlarged the interdiffusion coefficient of Cu_6Sn_5 but diminished the interdiffusion coefficient of Cu_3Sn at the interface. Hence,

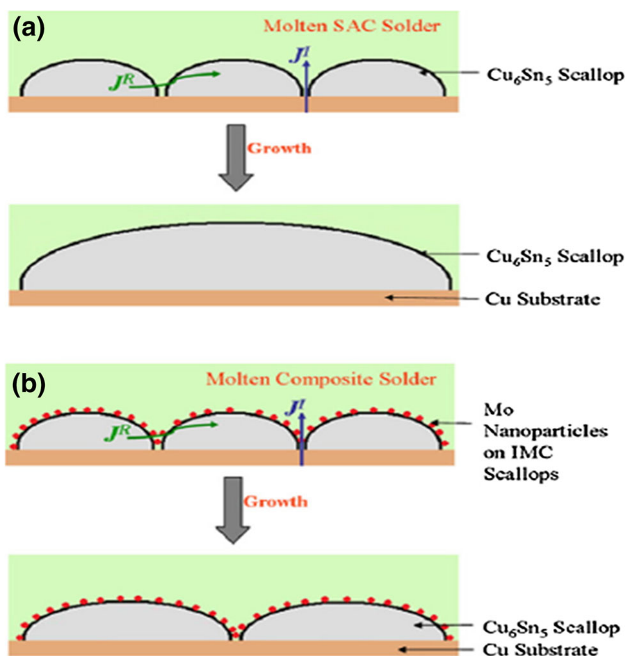

Fig. 13 Schematic diagram of scallop growth. **a** Sn–3.8Ag–0.7Cu solder, **b** Sn–3.8Ag–0.7Cu solder bearing Mo nanoparticles [34]

it is reasonable to conclude that this solid solution has a restraining effect on the interfacial Cu_3Sn growth [96]. Similarly, Ref. [41] reported that the presence of In in the interfacial system greatly influenced the growth kinetics of $Cu_3(Sn,In)$ (ε-phase) as well as the activation energy for the growth of ε-phase, while nearly had no effect on those of $Cu_6(Sn,In)_5$ (η-phase). The η-phase and ε-phase are two duplex IMC layer that gradually formed at the solder joint of Sn–3.0Ag–0.4Cu–7.0In/Cu subjected to isothermal aging at 180 °C. With aging time extending from 24 to 168 h, the amount of Kirkendall voids, dominated by Cu atom diffusion, ascend not only at Cu/ε interface but also inside ε layer, which potentially threaten the reliability of solder joints. Unlike elemental In or Pd addition, Ref. [97] disclosed that adding Sb (0–2.0 wt%) into Sn–3.5Ag–0.7Cu solder obviously interrupted Cu_6Sn_5 growth at the Sb-containing solder/Cu interface due to the grain boundary pinning effect caused by $Cu_6(Sn,Sb)_5$ and $Ag_3(Sn,Sb)$ IMCs located at the boundary of Cu_6Sn_5, as illustrated in Fig. 15. However, Sb addition slightly affected Cu_3Sn IMC growth at the corresponding interface. So, as aging time and temperature prolonged, the growth rate of interfacial Cu_3Sn layer was observed to be smaller than that of interfacial Cu_6Sn_5 layer.

Besides, Al [95] and Ga addition [20], albeit with low solubility, might also decrease Sn activity involved in the interfacial reaction. To be specific, the solder joint of Sn–Ag–Cu–1Al/Cu reflowed under the forming gas of 2 $\%H_2$ + 98 $\%N_2$ exhibited a η2 (AlCu) IMC layer due to relative rich Al quantity at the interface. This Al-containing IMC layer was able to reduce the growth rate of interfacial IMCs since it can decrease Sn activity. After staying at the interface for longer than 1 month, the unstable η2 phase migrated towards and gradually substituted the previously formed η (Cu_6Sn_5) and ε (Cu_3Sn) IMCs at the solder/Cu interface. Eventually, they transformed to δ (Al_2Cu_3) dispersed into the bulk solder again. Similarly, the reaction between molten Sn3.5Ag–0.7Cu–1.5 Ga and Cu substrate resulted in the formation of barrier layer (Cu_2Ga, Fig. 16b, d) on top surface of the original Cu_6Sn_5 IMC layer that could hinder the Cu or Sn diffusion in the vicinity of interface. So, the growth of interfacial IMC layers can be eventually retarded. After aging treatment at 180 °C for 4 days (Fig. 16c, d), Sn–3.5Ag–0.7Cu/Cu interface observed the presence of two visible IMC layers (Cu_6Sn_5 and Cu_3Sn), while only little Cu_3Sn phase appeared at Sn–3.5Ag–0.7Cu–1.5 Ga/Cu interface, suggesting minor Ga addition can disturb the interfacial Cu_3Sn growth.

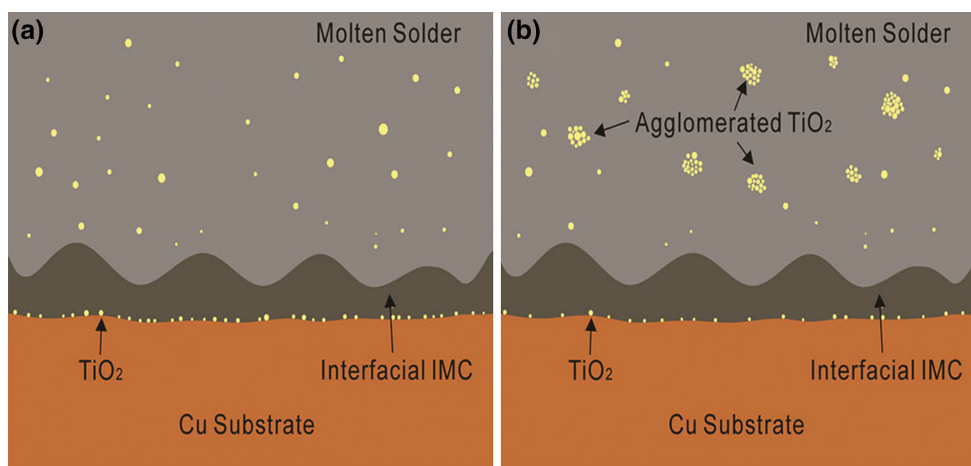

Fig. 14 Schematic diagrams of interfacial IMCs growth in Sn–3.0Ag–0.5Cu–TiO_2 solder [75]

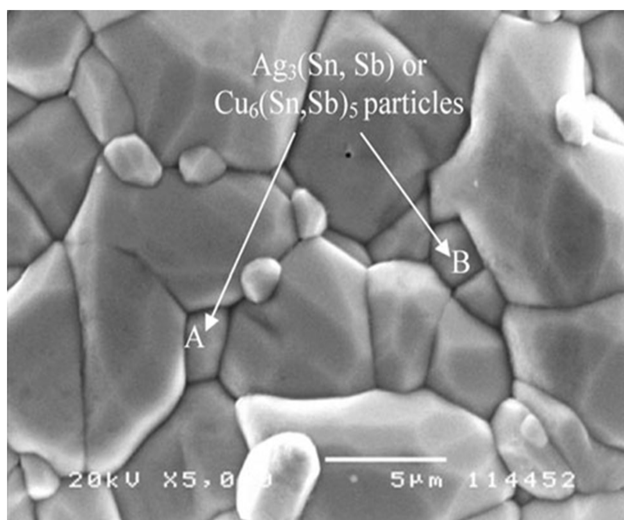

Fig. 15 Particles pinning along the grain boundary in Sn–3.5Ag–0.7Cu–1.0Sb aged at 150 °C for 600 h [97]

7 Mechanical properties of solder joints

As a significant role in the microelectronic packaging, solder joint must hold high strength to withstand thermal stress and accidental external impact during assembly and usage to meet the increasingly rigorous demands of integrated circuits particularly in today's extensive prevalence of 3D IC package [56, 77]. To a large extent, microstructural characteristics is obviously important in determining the mechanical performance of solder joint, which is also strongly influenced by the examined temperature and strain rate [40, 98]. Based on the mentioned-above presentations of microstructure alterations in Sn–Ag–Cu solders caused by alloys and nanoparticles addition, one can obtain plentiful changes in corresponding mechanical performance under various forms of mechanical loadings such as push, shear, pull, drop and indentation, which will be introduced in this section.

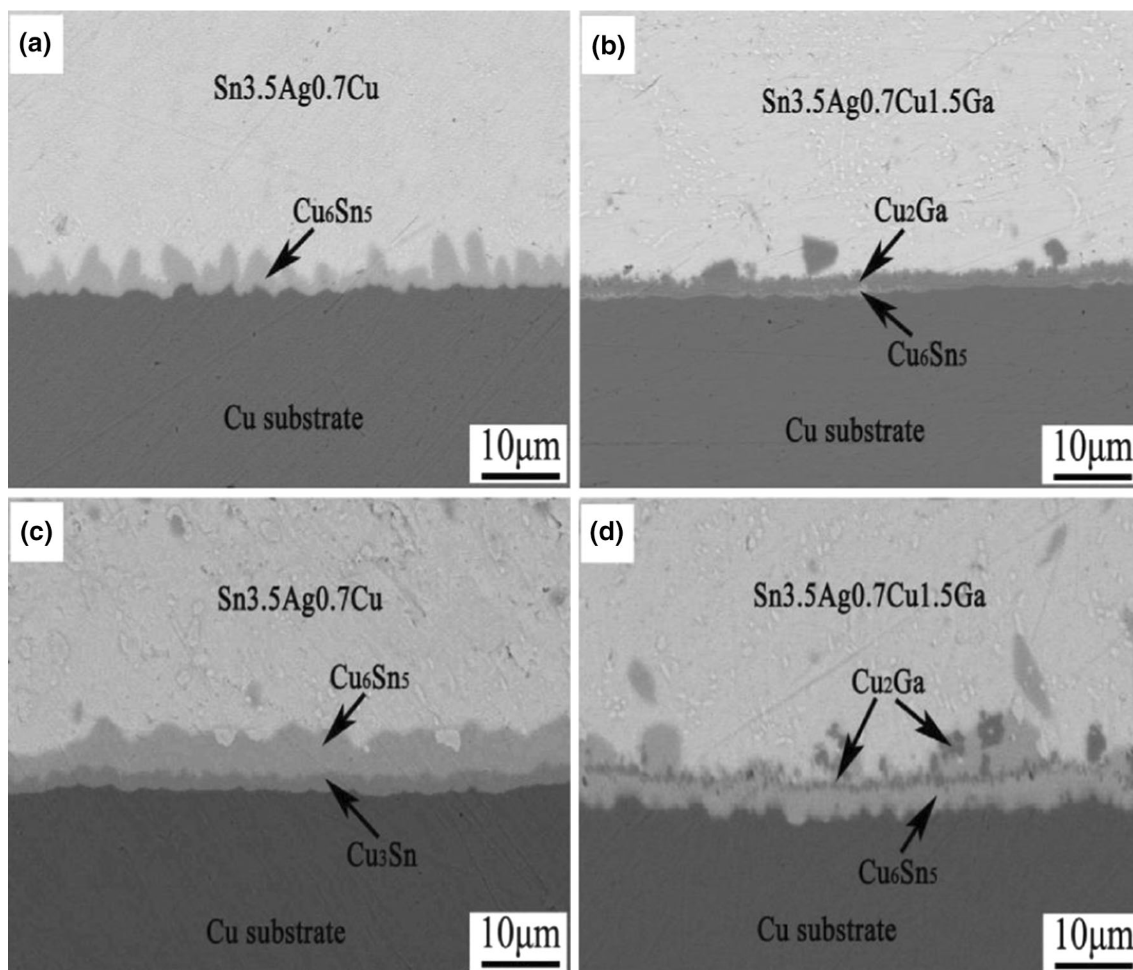

Fig. 16 Morphologies of as-reflowed **a** Sn–Ag–Cu/Cu, **b** Sn–Ag–Cu–Ga/Cu interface and aged **c** Sn–Ag–Cu/Cu, **d** Sn–Ag–Cu–Ga/Cu interface (180 °C, 4 days) [20]

Nanoparticles addition, particularly the non-reacting, non-coarsening ones, was confirmed to be one of the most effective and readily available approaches to improve the mechanical properties of solder joints. This can be accounted by the equation that calculate the critical shear stress (τ) which enable dislocations to bypass the second phase particle [99, 100], expressed as follows:

$$\tau = af^{1/2}r^{-1} \quad (2)$$

where a is a constant, f represents the volume fraction, and r is the radius of second phase particle. Apparently, a smaller second phase particle indicates higher critical shear stress necessary for dislocations to bypass the second phase particle. So, small Ag_3Sn particles in the solder matrix as well as particles with nano-size can impede the dislocation movements and eventually enhance the strength of solder joint. The most typical case is the Sn–3.0Ag–0.5Cu solder incorporated with refractory Y_2O_3 nanoparticles (0.25 wt%) which exhibited excellent thermal stability as well as satisfactory tensile strength. This satisfactory mechanical stability is correlated with the hamper of dislocation movements contributed by Y_2O_3 nanoparticles besides tiny Ag_3Sn IMCs [101]. In addition, Sn–3.0Ag–0.5Cu solder joint bearing 1 wt% ZrO_2 nanoparticles subjected to aging treatment at 150 °C for 30 days consistently exhibited higher shear strength and microhardness than non-aged solder joint. The shear strength stability is originated from factors such as incremental dislocation density at the interface of nano-reinforcing particles/solder matrix, hardening effect on the solder matrix and nano-ZrO_2 particulates with different rate. While, the hardness enhancement is attributed to the reinforcement effects contributed by homogeneously-distributed ZrO_2 nano-particles and the refined IMC particles (Ag_3Sn, Cu_6Sn_5). Besides, after a number of reflow cycles (1–16) in a reflow oven, ZrO_2 nanoparticles-containing solder joints observes only a slight change, which was related with the uniform distribution of ZrO_2 nanoparticles in the solder matrix [102]. Likewise, Sn–3.0Ag–0.5Cu incorporated with 0.5 wt% $SrTiO_3$ also exhibited a tiny disparity in shear strength after a few reflow cycles (1–16) or aging treatments (0–40 days, 150 °C). This is due to second phase dispersion strengthening effect as well as a controlled uniform dispersion of IMC particles (Cu_6Sn_5, Ag_3Sn and $AuSn_4$) throughout the β-Sn matrix. Besides, this uniform distribution of particles could also account for the ductile fracture morphology with an obviously rough surface possessed by the nano-composite solders [94]. Moreover, Al_2O_3 nanoparticles addition was capable to motivate a high nucleation density of stable second-phase dispersoid particles (Al_2O_3, Cu_6Sn_5 and Ag_3Sn) in the solder which serve as potential sites to pin grain boundaries as well as to increase dislocation densities and obstacles. So, the sliding of grain boundaries can be hindered and the dislocation motion will be restricted. It is why the shear strength of Sn–3.5Ag–0.5Cu solder bearing 1 wt% Al_2O_3 nanoparticles were reinforced by 14.4 and 16.5 % after 1 and 8 reflow cycles, respectively, when compared to those of pure solder joint [103].

Effects of alloying elements (e.g., RE, Bi, Ni, Ga, Al, Fe) on the mechanical properties of Sn–Ag–Cu solder are not that obvious in comparison to that of nanoparticles addition, but still have significant practical importance. The representative case is the Sn–Ag–Cu solder with Eu addition, whose shear and tensile strength simultaneously reach the maximum value when Eu content approaches to 0.04 wt%, as illustrated in Fig. 17 [22]. However, a further Eu addition beyond 0.04 wt% sharply weakened the mechanical strength because of bulk Sn–Eu phase oxidation which was a potential contaminant to the mechanical properties of solder joint. Similar trend between RE content and mechanical properties (shear or tensile strength) was also found for Sn–Ag–Cu–Yb [60] and Sn–3.8Ag–0.7Cu–Pr [25] (Nd [3]) solder joints. Therefore, strict management of RE content appears to be significantly essential to maximize their enhancement in relative mechanical properties of solder joints. In order to improve the comprehensive performance of Bi- and Ni-containing low-Ag Sn–Ag–Cu solder, Liu et al. [104] optimized the Bi and Ni concentration in the solder by using solders of Sn–0.7Ag–0.5Cu and Sn–3Ag–0.5Cu as contrast. The shear behavior of alloys indicated that Sn–0.7Ag–0.5Cu–3.5Bi–0.1Ni/Cu solder joint with a much smaller grain size of interfacial IMCs showed higher shear strength than that of other Sn–Ag–Cu/Cu solder joints with varied compositions. Besides, Sn–3Ag–0.5Cu/Cu solder joint exhibited a higher shear strength than Sn–0.7Ag–0.5Cu/Cu solder joint since high Ag concentration increased the number of Ag_3Sn nanoparticles adhered on Cu_6Sn_5 protrusions that could enlarge the bonding surface area with Cu substrate.

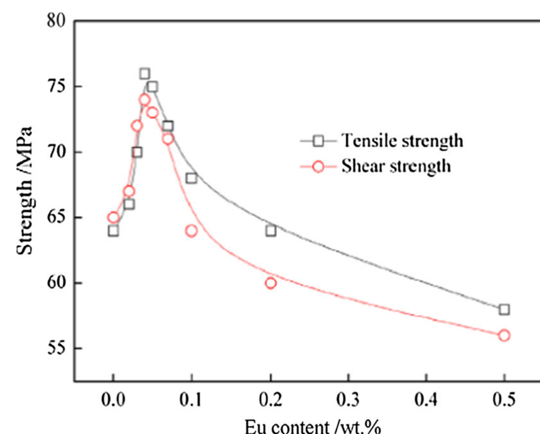

Fig. 17 Mechanical properties of Sn–Ag–Cu–xEu (x = 0–0.5 wt%) solder joints [22]

However, alloying Fe [95] or Al [105] into relevant Sn–Ag–Cu solders were not that satisfactory in strengthening the mechanical properties of solders due to the formations of large amount of bulk IMCs (e.g., $FeSn_2$, Al–Ag, Al–Cu IMCs) in the Sn-rich matrix that might potentially initiate cracks during the early tensile stage.

Also, solder alloys usually exhibit a susceptibility to strain rate and temperature during tensile test, where solders generally experience procedures of work hardening and dynamic recovery [88, 106], as reasonable concluded from Tables 6 and 7. It can be obtained that both values of UTS and YS of solders increase as the strain rate rises at a given temperature, in accordance with the fact that work hardening dominates relative to the dynamic recovery under this circumstance. This phenomenon is related to the interaction between IMCs or precipitates with dislocation activities. To be specific, at low strain rate, the precipitates in the solder can impede the dislocations moving fast, whereas with the strain rate rising up, these IMCs cannot capture the moving dislocations with larger velocity any more. So it resulted in the dislocations gliding on the slip planes that could tolerate the deformation [98]. Meanwhile, the UTS of solders doped with alloy or nanoparticles is still higher than that of pure solder even with strain rate increasing due to the extra incremental restraint to dislocation motions contributed by newly formed particles like $(Cu,Ag)_5Zn_8$ [107], SWCNT [108], ZnO [109], $(Cu,Ni)_6Sn_5$ phases [110], or nanoparticles themselves (SiC [38]). This explanation can also account for slower decrement in UTS and YS of composite solders than those of their monolithic counterparts with temperature elevating at a given strain rate during tensile deformation process. It is well-known that the mechanical behaviors at different temperatures are critical thermomechanical properties since high temperature can easily encourage recovery and softening procedures at a constant strain rate, allowing dynamic recovery to dominate over work hardening during tensile deformation. Therefore, dislocations can obtain much more energy to overcome small IMCs in Sn-rich matrix, thus causing a reduction in both values of UTS and YS [108, 110]. However, the elongation of ductile materials does not always increase or decrease with either temperature elevation or strain rate decrement, and the prime ductility can be attained at a certain temperature and strain rate. This is attributed to the piecewise discontinuous and heterogeneous material structure caused by the emerging micro-defects or damage. Hence, deep investigations of the physical properties of IMC chemistries, impurity segregation to interfaces, the nature of interface formed between IMCs and matrix remain to be done to understand this trend thoroughly.

Table 6 The effect of strain rate on the UTS (MPa), YS (MPa) and El (%) of solder alloys

Mechanical parameters Strain rate (s^{-1})	UTS (MPa)	YS (MPa)	El (%)
Sn–1.0Ag–0.3Cu/Sn–1.0Ag–0.3Cu–3Zn [107]			
5×10^{-5}	19.62/24.85	18.71/22.97	57.54/61.1
3.3×10^{-4}	22.15/27.41	21.54/25.39	74.34/87.89
5.4×10^{-4}	23.46/29.03	22.95/27.28	49.01/55.47
1.15×10^{-3}	26.19/31.46	24.47/28.76	83.50/87.83
2.9×10^{-3}	27.41/35.232	25.78/33.48	77.09/81.35
Sn–1.0Ag–0.5Cu/Sn–1.0Ag–0.5Cu–0.35SiC [38]			
10^{-4}	29.0/32.0	26.3/29.2	15.5/13.2
10^{-3}	30.0/33.2	28.8/31.3	12.3/13.0
Sn–3.8Ag–0.7Cu/Sn–3.8Ag–0.7Cu–0.1SWCNT [108]			
5×10^{-4}	28/37	28/34	38.7/45.0
5×10^{-3}	52/58	44/57	23.0/22.2
5×10^{-2}	63/67	61/67	20.5/20.2
Sn–3.0Ag–0.5Cu/Sn–3.0Ag–0.5Cu–0.7ZnO [109]			
1×10^{-4}	20.7/29.59	18.31/26.31	_
5×10^{-4}	24.36/33.68	23.35/31.33	_
1×10^{-3}	30.94/39.85	28.99/37.02	6.5/4.7
5×10^{-3}	36.81/43.55	34.78/39.88	_
1×10^{-2}	40.55/49.50	38.13/47.68	_

"/" and "_" represents space character and no recorded data, respectively

8 Creep behaviors

Actually, what researchers truly concerned about is how to eliminate the (cyclic) thermal stress at the solder joint built up in thermal service, where the solder joint might experience typical creep deformation due to the high homologous temperature involved. Even more serious is that the room temperature (T), about 298 K, can reach about 0.6 times of the T_m of Sn–Ag–Cu solder, indicative of a distinct high temperature creep performance. Besides, different coefficients of thermal expansion (CTE) between chip and metallic coatings or substrates also become one of the major factors that may trigger low cycle fatigue [7, 22, 57, 58]. Generally, a representative creep curve consists of three regimes: primary, secondary (or steady-state), and tertiary regime. The creep behaviors of solder alloy highly depend on the secondary regime, where the creep strain rate is assumed to retain stable with time extending due to a dynamic balance between strain-hardening and recrystallization (softening) in this stage. Therefore, models built up to describe creep behavior can be simplified then. Although laws describing the creep deformation behaviors over a wide range of stresses are

Table 7 The effect of temperature on the UTS (MPa), YS (MPa) and El (%) of solder alloys

Mechanical parameters Temperature	UTS (MPa)	YS (MPa)	El (%)
Sn–1.0Ag–0.3Cu/Sn–1.0Ag–0.3Cu–3Zn (strain rate $\varepsilon = 1.15 \times 10^{-3}\ s^{-1}$) [107]			
25	26.19/31.46	24.47/28.76	83.5/87.83
50	18.61/24.12	17.5/23.27	36.45/41.14
70	16.74/22.55	16.51/21.94	62.19/42.67
90	15.52/19.71	14.84/18.12	37.25/50.17
110	12.95/17.95	12.54/17.39	41.18/39.41
Sn–1.0Ag–0.5Cu/Sn–1.0Ag–0.5Cu–0.35SiC (strain rate $\varepsilon = 1 \times 10^{-3}\ s^{-1}$) [38]			
25	30.0/33.2	28.8/31.3	12.3/13.0
75	21.9/23.2	19.0/19.4	16.0/15.3
Sn–3.8Ag–0.7Cu/Sn–3.8Ag–0.7Cu–0.1SWCNT (strain rate $\varepsilon = 5 \times 10^{-3}\ s^{-1}$) [108]			
25	52/58	44/57	23.0/22.2
50	47/50	31/38	15.3/17.8
75	38/43	27/28	30.2/28.4

"/" and "_" represents space character and no recorded data, respectively

various, the following Garofalo hyperbolic-sine law is the most universally accepted [43, 111, 112]:

$$\dot{\varepsilon} = A[\sinh(\alpha\sigma)^n \exp(-Q/RT)] \quad (3)$$

where ε' is the creep rate, related to both temperature (T) and activation energy (Q), A is material constants, σ is the applied stress, n represents creep stress exponent, and R stands for universal gas constant. Generally speaking, if temperature and strain rate are ascertained, a larger value of Q or n indicates higher creep resistance of a certain solder [42]. Table 8 lists a series of n and Q values for Sn–Ag–Cu–X composite solders (X = Ni, Zn, Sb, etc.) at room temperature (25 °C). Apparently, solders with suitable content of alloys addition perform more enhancive creep resistance than their monolithic counterparts due to their higher capacity to impede dislocation movements, as can be obtained in Table 9. Additionally, n-value is known to depend on the microstructure and highly determines the creep deformation mechanism. That is, dislocation mechanism dominates due to viscous glide ($n \approx 3$) or dislocation climb ($n > 4$), while diffusion mechanism takes effect with n-value close to 1, and n-value next to 2 stands for grain boundary sliding [98]. So, according to the n-values of various solders ($n > 4$) listed in the Table 8, it is suggested dislocation mechanism dominates the creep deformation in all of these composites at room temperature.

Alloys addition especially RE addition can also distinctly slow down high temperature degradation in creep resistance. For instance, a creep test of Sn–Ag–Cu–Eu solder under the load of 15 MPa at 55 °C with the application of small single shear-lap joint was conducted by Zhang et al. [22]. The experimental results indicated that minor Eu addition, especially rising up to 0.04 wt%, distinctly prolonged the creep rupture life of solder joint. As can be seen from Fig. 18, the creep rupture life of Sn–Ag–Cu–0.04Eu solder was prolonged up to 8.5 times longer than that of original Sn–Ag–Cu solder. This can be attributed to the blocks of dislocation movements caused by newly formed particles such as EuSn3, precipitated IMCs of Cu_6Sn_5 and Ag_3Sn [98].

Besides, when compared with aforementioned alloys addition, nanoparticles addition was confirmed to be more effective to enhance the creep resistance of Sn–Ag–Cu solders since they can provide effective obstacles for

Table 8 The effects of additives on the values of Q and n at room temperature (25 °C)

Sn–Ag–Cu/Sn–Ag–Cu–X solder	α (MPa^{-1})	Q (KJ/mol)	n
Sn–0.5Ag–0.7Cu/Sn–0.5Ag–0.7Cu–0.05Ni [7]	0.05741/0.05385	52.4/56.6	7.4/8.5
Sn–1.0Ag–0.3Cu/Sn–1.0Ag–0.3Cu–3.0Zn [43]	0.05000/0.04937	45.0/48.0	6.0/7.5
Sn–1.0Ag–0.5Cu/Sn–1.0Ag–0.5Cu–0.06Ni [47]	0.03739/0.04135	40.7/46.0	7.0/8.4
Sn–1.0Ag–0.5Cu/Sn–1.0Ag–0.5Cu–0.5Sb [56]	0.03739/0.43243	40.7/54.4	7.0/9.3
Sn–1.0Ag–0.5Cu/Sn–1.0Ag–0.5Cu–0.35SiC [38]	0.05578/0.05782	45.1/48.4	6.1/7.3
Sn–2.0Ag–0.5Cu/Sn–2.0Ag–0.5Cu–0.05Ni [42]	0.05578/0.05782	76.2/84.6	7.8/8.8
Sn–2.0Ag–0.5Cu/Sn–2.0Ag–0.5Cu–0.5Zn [42]	0.05578/0.06363	76.2/88.3	7.8/9.7

"/" represents space character

Table 9 The effects of additives on the creep behaviors of Sn–Ag–Cu solder alloys

Sn–Ag–Cu based solders	Creep behaviors
Sn–0.5Ag–0.7Cu–Ni [7]	The creep rupture life of 0.05 wt%-doped solder is evidently prolonged, about 2.0 times longer than that of plain solder and about 5.0 times better than that of the solder doped with 0.1 wt% Ni
Sn–1.0Ag–0.3Cu–Zn [43]	The creep life time and the creep resistance of Sn–1.0Ag–0.3Cu–3Zn solder were two times and 360 % higher than that of unreinforced solder, respectively
Sn–1.0Ag–0.5Cu–Sb (Ni) [56]	With 0.06 wt% Ni or 0.5 wt% Sb addition, significant improvements in creep resistance (210 and 350 %) of the composite solder were realized. Meanwhile, the creep life time of Sn–1.0Ag–0.5Cu–0.5Sb was 2–3 times higher than that of the non-added solder
Sn–2.0Ag–0.5Cu–Zn (Ni) [42]	0.5 wt% Zn or 0.05 wt% Ni addition witnessed an ascending trend in creep resistance of composite solders, giving a 450 % and 190 % increase, respectively, compared to the plain solder
Sn–Ag–Cu–Eu [22]	With 0.04 wt% Eu addition, the creep rupture life and the thermal fatigue life were 8.5 times and 37.4 % higher than those of monolithic solder, respectively
Sn–3.5Ag–0.5Cu–ZnO [31]	A distinct improvement in the creep resistance was achieved by adding 0.5 wt% ZnO to the plain solder

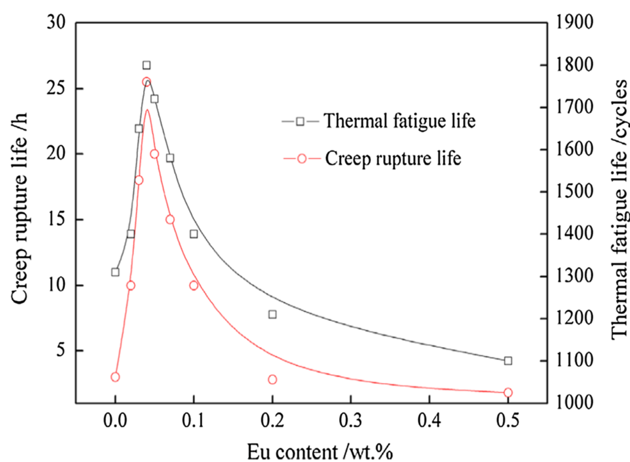

Fig. 18 Creep rupture life and thermal fatigue life of Sn–Ag–Cu–xEu (x = 0–0.5 wt%) [22]

gliding dislocations to move across [113]. When examining the alterations in creep properties influenced by nanoparticles addition, depth-sensing indentation test is generally applied, which is a widely-used method to characterize mechanical properties of small structure as well as determine the indentation load and depth during indentation sequence at various temperatures. From the curves of indentation load versus displacement, one can obtain the indexes of creep evaluation (n and Q), hardness and Young's modulus of investigated samples. For instance, Fig. 19 [114] shows the typical load-depth curves of Sn–3.5Ag–0.7Cu solder bearing Ni–CNTs with the maximum load of 40 mN and the holding time of 120 s. As can be seen, after adding 0.05 wt% Ni–CNTs, the creep penetration depth was distinctly declined, from 477 to 299 nm, indicative of an evidently improved creep resistance. This could be attributed to the strong adhesion between solder matrix and Ni–CNTs that in turn allows for effective load transfer. Additionally, single walled carbon nanotubes (SWCNT; diameter: 1.2 nm, length: 5–10 μm) produced by vapour deposition technique with the advantage of relative higher elastic modulus (1–3 TPa) than high strength steels were used to synthesize composites through powder metallurgy route. Its creep behaviors indicated that an increment in SWCNTs (up to 0.1 wt%) addition into Sn–3.8Ag–0.7Cu contributed to an enhancement in the creep resistance due to the reduction in the steady state rate as well as primary creep stage displacement and primary creep stage time. This was probably associated with the load sharing by SWCNTs and the interactions of the dislocations with these SWCNTs [108]. Moreover, nanoparticles addition also has a great effect on the thermal degradation in creep resistance. For instance, whether for plain Sn–1.0Ag–0.5Cu solder or for SiC-containing solder, the creep resistance of solders receded under a relative high temperature environment according to their declined n-value. However, over the whole examined temperature range (25, 70 and 120 °C), the n-values of Sn–1.0Ag–0.5Cu–0.35SiC solder were larger than those of plain solder, which was probably due to the limitations of dislocation climbings caused by the interactions of dislocations with the fine IMCs [33].

9 Reliability

With recent trend of higher density of electronic circuits in modern electronic devices especially in this new era of 3D IC package, it is of critical importance to ensure the reliability of micro solder joints since they serve as mechanical supports as well as electrical interconnection within the solder devices [1, 115]. Therefore, it becomes utmost

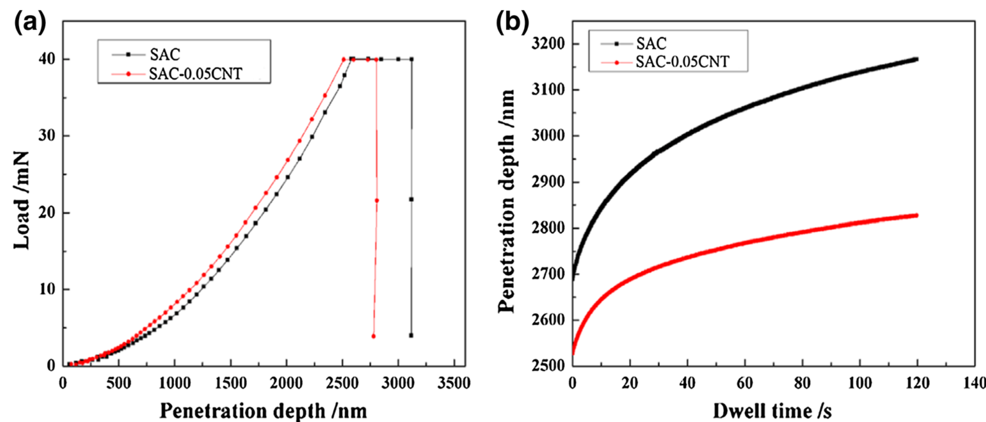

Fig. 19 **a** The load-depth curves and **b** changes of penetration depth for Sn–3.5Ag–0.7Cu–xNi–CNT (x = 0, 0.05 wt%) solders (maximum load: 40 mN, holding time: 120 s) [114]

essential to examine reliability susceptibility of micro solder bonding to various wretched conditions and to early estimate their reliability fatigue lives [15, 96, 116]. The method of micro-alloying was found helpful in enhancing the reliability of original solder joint subjected to various forms of external factors, such as (cyclic) mechanical loading, (cyclic) thermo-mechanical loading, high temperature aging. In this section, different reliability failure modes of Sn–Ag–Cu solder joint under severe environments are introduced.

Failure mode of thermal cycling (TC) degradation besides high temperature aging introduced in Sect. 6 is one of the major reliability concerns that should be attached importance to. Usually, this thermally induced deformation and stress originate from frequent behaviors of turn-on and turn-off within a short time span [117]. It has been extensively confirmed that solder joints with alloys addition exhibited more enhancive reliability than their monolithic counterparts. For instance, minor quantity of Zn (0.4 and 1 wt%) was melted into both Sn–1.0Ag–0.3Cu and Sn–1.0Ag–0.1Cu solders to investigate thermal shock behaviors of corresponding solder joints with a typical temperature profile (TC range −40 to 125 °C, dwell time 30 min). The results showed that Sn–1.0Ag–0.3Cu–1Zn solder joint exhibited the highest thermal shock resistance along with the lowest susceptibility to both solder deformation and crack initiation among all the examined samples, which was associated with the flow stress of solder alloys [14]. Similarly, TC reliability tests (TC range −55/125 °C; dwell time 15 min) of Sn–1.0Ag–0.5Cu solder joints doped with Pd, Zn, Ti were conducted by Son et al. [16] to measure the thermal fatigue life of the corresponding solder joints. The experimental results indicated that almost all the doped solders exhibited more enhancive TC reliability than non-doped ones regardless of the different pad finish material on the BGA side (NiAu/Cu–OSP units, (b) Cu–OSP/Cu–OSP units). In particular, Sn–1.0Ag–0.8Cu–Ti displayed a superior performance with almost three times of higher reliability than Sn–1.0Ag–0.5Cu solder at the Cu–OSP/Cu–OSP unit. This is due to the suppressive effect on dislocation motions caused by second-phases produced in thermal storage as well as precipitated IMCs in bulk solder. Moreover, RE addition to Sn–Ag–Cu solders was also demonstrated to have visible repercussions in thermal fatigue lives. For instance, it was found Eu addition with optimal content could prolong the thermal fatigue life as well as creep rupture life in the reliability test, as already introduced in Sect. 8 [22]. As Eu content rose to 0.04 wt%, both creep rupture life and thermal fatigue life of RE-containing solder would be maximized to 8.5 times and 37.4 % longer than those of monolithic solder, respectively. This is due to the blocks of dislocation movements caused by $EuSn_3$ precipitates particles as well as the refined Cu_6Sn_5 and Ag_3Sn. Moreover, Zhang et al. [118] studied the influence of Al nanoparticles on the TC reliability of Sn–Ag–Cu solder joints subjected to cycling temperature in a three-zone chamber (TC range −55/125 °C; cycle time 56 min; JEDEC standard). The reliability results showed that both as-soldered and thermally-cycled solder joint incorporated with Al nanoparticles in QFP devices exhibited evidently stronger tensile force as well as longer fatigue life than their monolithic counterparts since nanoparticles themselves can act as obstacles to restrain the movements of grain boundaries and dislocations.

Different from thermal fatigue induced by mutative temperature field, thermomechanical fatigue is aroused by a coupling effect of external temperature and stress field, which is also one of the major reliability issues present in electronic devices that should be taken seriously [119, 120]. A custom built thermomechanical micro (TMM) scale test with a strain rate of 5.5E − 2 (1/s) at

room temperature was conducted to investigate the influences of separate addition of 0.05 wt% Mn and 0.55 wt% Sb on cyclic mechanical durability of Sn–1.0Ag–0.5Cu solder joint. The examined results showed that neither 0.05 wt% Mn nor 0.55 wt% Sb definitely improved the cyclic mechanical durability of the solder joint [121]. The thermal fatigue behavior of Sn–Ag–Cu–xYb solder joints (x = 0–0.1) in QFP256 assembly tested by TL-100 thermal cycle equipment was investigated with the imposed thermal cycle loading ranging from 218 to 398 K and dwell time of 15 min. The corresponding results were shown Fig. 20 [60]. As can be seen, with minor Yb addition (0–0.05 wt%), the fatigue life of Sn–Ag–Cu–xYb solder joints is distinctly prolonged with the maximum value realized for 0.05 wt% Yb-doped solder joint. This fatigue life variation can be explained based on the creep theory that small Sn–Yb particles formed in the matrix can not only remarkably increase the number of dislocations, but can also hinder the dislocation motions during creep deformation. Moreover, an automated TMA 2940 thermomechanical analyzer was utilized to measure the CTE of the Sn–3.5Ag–0.7Cu–xNi–CNTs (x = 0–0.05 wt%) samples via calculating the displacement of them as a function of temperature ranging from 50 to 150 °C. The measured results showed that solder incorporated with CNTs exhibited a lower CTE value than its monolithic counterpart, so that it can effectively maintain the thermal stability of composite solders. Also, it was confirmed both as-soldered and thermally cycled solder joint incorporated with 0.05 wt% Ni–CNTs (up to 2000 cycles; 40–125 °C) with the application of Ni/Au finished Cu substrates displayed superior ultimate shear strength to their monolithic counterparts. Figure 21 [122] illustrates the SEM micrographs of fracture surfaces of the shear specimens subjected to thermal cycles. As can be seen, an obvious ductile fracture mode was exhibited due to the accommodation of thermal

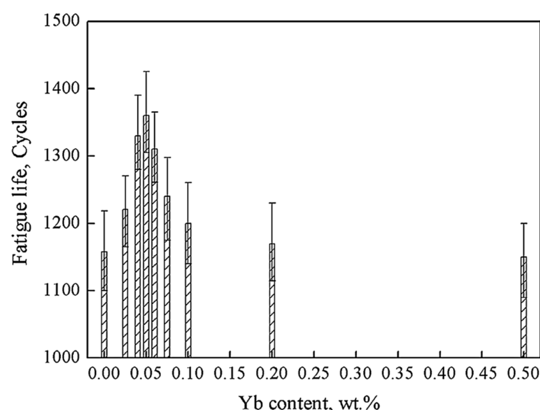

Fig. 20 The fatigue life of SnAgCu–xYb (x = 0–0.5 wt%) solder joints [60]

and elastic modulus mismatch contributed by geometrically necessary dislocations, load-transfer resulting from the existence of Ni–CNTs, as well as thinner IMC layer at the composite solder bonding.

Recently, a rapid growth of hand held electronic devices production, such as cell phones, PDAs and Netbooks, have made the drop impact reliability more noteworthy than other reliability concerns in case of accidental drops or impacts that might cause the package breakage [51, 123]. Elemental Pd has recently become popular in improving the reliability of microelectronic solder joints not only because of the extensive application of Pd (or Pd-P) surface finish on Ni(P) metallization pads but also due to the avoidance of hyper-corrosion of Ni(P) pads (generally termed as "black pads"). For instance, Yu et al. [124] assessed the drop/shock reliability of the Sn–1.2Ag–0.7Cu–0.4In solder joints with 0.03 wt% Pd addition via dropping a rod (weight: 30 g; drop height: 100 mm) onto the backside of PWB using a self-made rod drop impact tester with the failure criterion set as 100 Ω. The experimental results exhibited that a Sn–1.2Ag–0.7Cu–0.4In–0.03Pd solder performed superior drop/shock reliability due to the excellent fracture energy, followed by Sn–1.0Ag–0.5Cu, Sn–1.2Ag–0.7Cu–0.4In and finally Sn–3.0Ag–0.5Cu solder. Additionally, a high-speed ball shear (HSBS) test (shear speed: 2 m/s) was conducted by Ho et al. [96] to investigate the mechanical response of Sn–3Ag–0.5Cu solder bearing Pd (0–1 wt%). This shear reliability results displayed a degradation in mechanical strength of Sn–3Ag–0.5Cu–xPd/Ni solder joints with the enlargement of x, particularly when x exceeded 0.3 wt%, which was associated with the formation of $(Pd,Ni)Sn_4$ IMCs on top surface of $(Cu,Ni)_6Sn_5$ IMC layer, as illustrated in Fig. 22. Nevertheless, it was found that an increase in Cu and Pd content to 1 and 0.5 wt%, respectively, contributed to a suppressive effect on $(Pd,Ni)Sn_4$ growth, so that the occurrence of Pd embrittlement in the solder joints could be avoided. Moreover, Son et al. [16] conducted a drop impact investigation (acceleration peak: 1500 g; duration time: 0.5 ms) of Sn–1Ag–0.5Cu–Zn, Sn–1Ag–0.5Cu–Pd, Sn–1Ag–0.8Cu–Ti, Sn–1Ag–0.8Cu–In–Sb–Ni solders. It showed that only the doped Ti solder was capable to enhance the drop impact reliability regardless of pad finish (NiAu/Cu–OSP or Cu–OSP/Cu–OSP) on the Ball Grid Array (BGA) side. In the case of Cu–OSP/Cu–OSP unit, the doped Ti solder did not fracture until the 200th time in the drop test. Furthermore, nanoparticles of SiC addition into Sn–1.0Ag–0.5Cu solder was also demonstrated to play an important role in enhancing the drop impact performance due to the increased elastic compliance and plastic energy dissipation ability of the bulk solder [51].

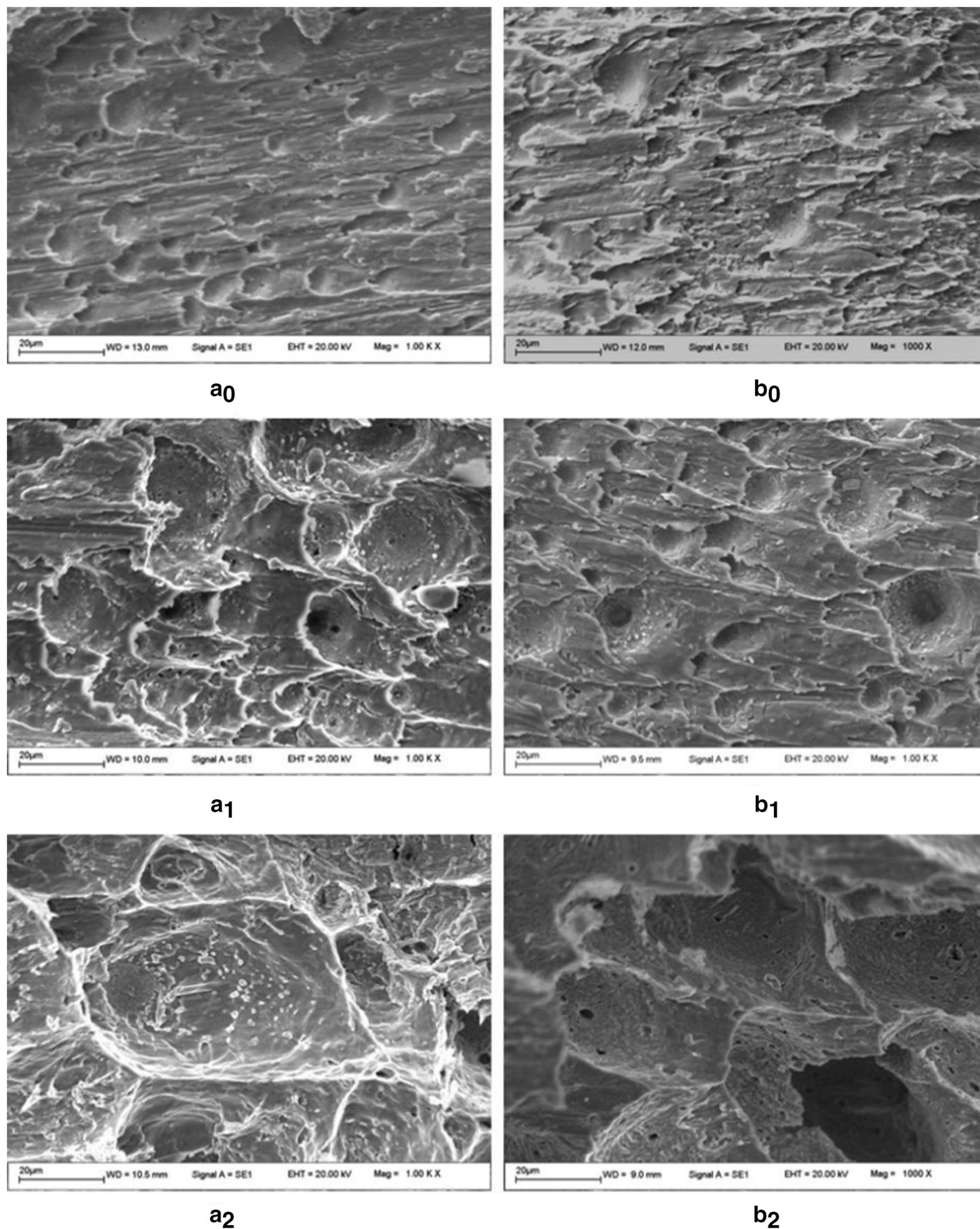

Fig. 21 Typical SEM images of: **a** plain Sn–3.5Ag–0.7Cu and **b** Sn–3.5Ag–0.7Cu–0.05Ni–CNT solder joint with Subscripts 0, 1 and 2 denote thermal cycling for 0 cycle, 1000 cycles, and 2000 cycles, respectively [122]

10 Electromigration (EM) and thermomigration (TM)

Nowadays, with the urgent demands for higher performance of portable electronic devices, the dimension of solder bump keeps decreasing, thus leading to a considerable rise in current density within each micro interconnection. Consequently, the EM phenomenon became more prone to occur than before, which is a process of directional atomic movement, driven by a large momentum exchange from conducting electrons under the stressed current [125]. It can be concluded from a mount of

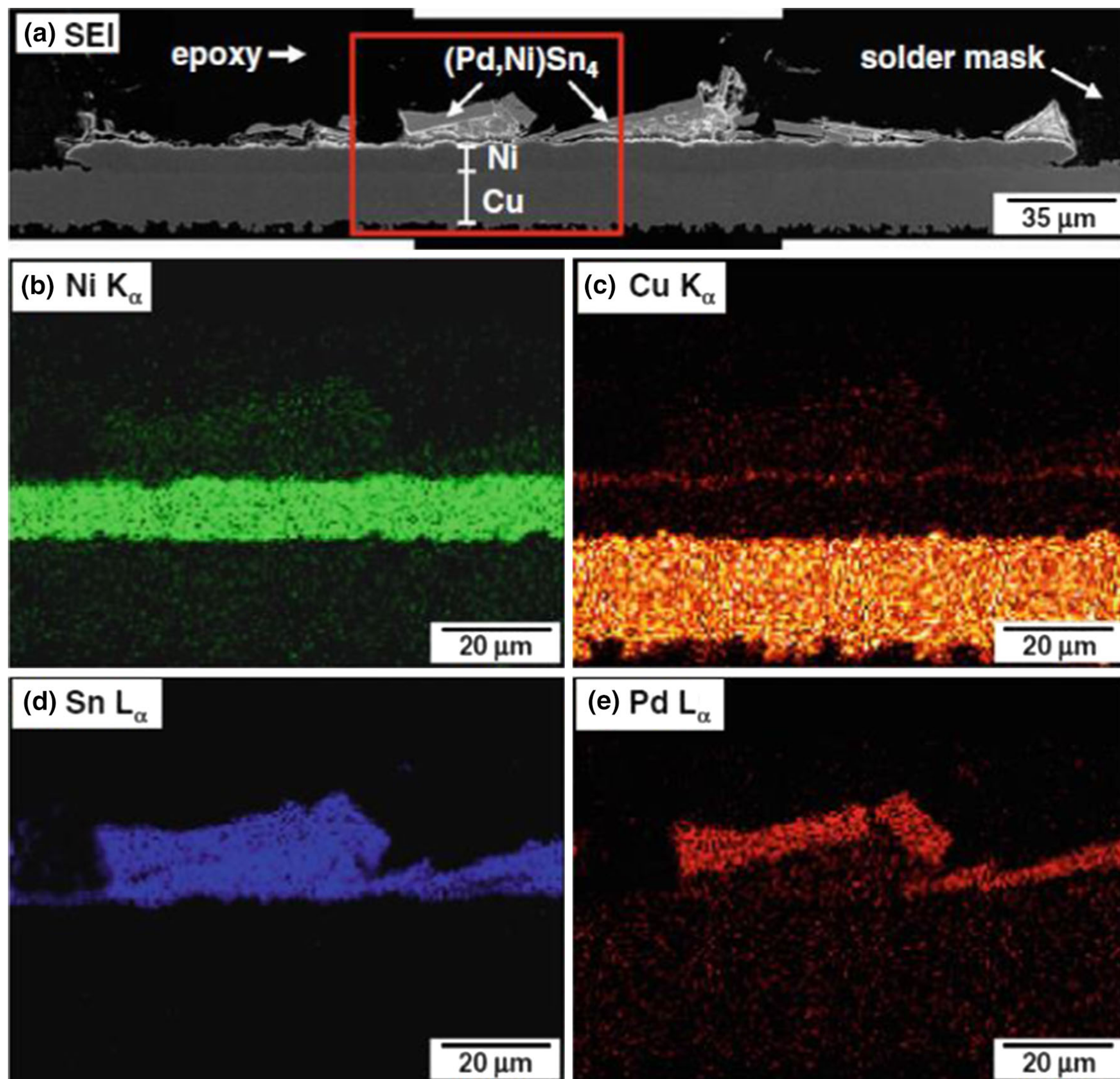

Fig. 22 **a** Electron micrograph of the cross-sectional Sn–3Ag–0.5Cu–0.5Pd/Ni joint (board side) after the HSBS test; **b–e** EDX X-ray images (Ni Ka, Cu Ka, Sn La, and Pd La) corresponding to (**a**) [96]

research that current-induced Cu diffusion is the dominant EM failure mode in Sn–Ag–Cu solders, in contrast to dominant diffusing specie of Pb in eutectic Sn–Pb solder under the stressed current [126]. Since directional atomic transportation may causes the microstructural variations in micro interconnection, several electrical failures may be triggered, such as voids and crack formation, phase separation, solder extrusion/whiskers, IMC growth disturbance, and under bump metallization (UBM) consumption [127, 128]. Even more serious is that at the area of current crowding where EM phenomenon easily occurs, thermal gradient might be generated and rapidly rose up to the highest level when electronic devices were in service [129]. As a result, thermomigration, an accelerated mass atom transport phenomenon in metal driven by thermal gradient, might occur accompanying with EM, which can also disturbed the interfacial IMCs growth [130, 131]. Besides, when stressed with high density current, the flip chip solder bump in commercial BGA product also observed the generation of compositional gradient driving force, induced by asymmetrical composition distribution after phase segregation [132]. Hence, the total mass transport under the coupled field can be expressed as:

$$J_{tot} = J_{em} + J_{st} + J_{th} = \frac{CD}{kT}\left[Z^{*}e\rho j - \Omega f\frac{\partial\sigma}{\partial x} - \frac{Q^{*}}{T}\frac{\partial T}{\partial x}\right] \tag{4}$$

where J_{em}, J_{st}, J_{th} stand for the EM atomic flux, the compositional gradient atomic flux and the TM atomic flux, respectively, C and D represent the concentration of diffusing atoms, thermally activated diffusion coefficient, respectively, k is the Boltzmann's constant and T is the

average temperature. In addition, three terms in the brace of Eq. (3) correspond to EM driving force (F_{em}), compositional gradient driving force (F_{st}) and TM driving force (F_{th}), respectively, expressed as [133]:

$$F_{em} = Z^{*} e \rho j \tag{5}$$

$$F_{st} = -\Omega f \frac{\partial \sigma}{\partial x} \tag{6}$$

$$F_{th} = -\frac{Q^{*}}{T} \frac{\partial T}{\partial x} \tag{7}$$

where Z^* and Q^* are two particularly important parameters, signifying effective charge number of the migrating ions in EM and the constant activation energy in TM, respectively. If the values of Z^* and Q^* are known, the driving forces of both EM and TM (F_{em}, F_{th}) can be calculated then [132, 134]. In general, 1×10^4 A/cm^2 and 1000 °C/cm are two widely accepted threshold values that can simultaneously induce the phenomena of EM and TM, so that they can be used to calculate the driving forces for EM and TM ($F_{em} = 1.6 \times 10^{-17}$ N; $F_{th} = 0.4 \times 10^{-17}$ N), respectively [135–137]. Research on TM hasn't been that mature yet since it still stayed at the initial stage of investigating the dominant diffusion species in different solder systems, including Sn–Pb, Sn–Ag, Sn–Zn, Sn–Bi and Sn–Ag–Cu, etc. However, the EM issue occurring in Sn–Ag–Cu solder joint caused by high current density was found ameliorated by incorporating certain additives into Sn–Ag–Cu solders [138, 139].

Alloys of Co [139], Ni [140], Ge [141], Zn [142] which own the similar radius as Cu atom, were found having a suppressive effect on current-induced EM issue. For instance, no conspicuous EM damages emerged in Sn–3.0Ag–0.5Cu–xCo (0, 0.05 and 0.2 wt%) solder matrix under the stressed current of 10^4 A/cm^2 at 50 °C for 16 days since Co can act as diffusion barrier to retard the polarity effect. However, after stressed with high density current at 150 °C for 1 day, Sn–3.0Ag–0.5Cu solder joint displayed two distinct wave-type of Cu_6Sn_5 and Cu_3Sn IMC layers with little Sn phases inside it at the cathode side, but only one single layer of Cu_6Sn_5 at the anode side, as shown in Fig. 23a, b. Three days later, two previous IMC layers (Cu_6Sn_5 and Cu_3Sn) combined into one notable IMC layer with planar-type at the cathode side. Besides, voids at the anode side moved away towards the cathode side driven by the motion and condensation of vacancies (Fig. 23c). At the anode side, Cu_3Sn emerged with Sn phases interior of this IMC layer between Cu_6Sn_5 and Cu substrate (Fig. 23d). In addition, Lee et al. [138] discovered that an individual Bi addition will not help relieve the polarity effect occurred in Sn–3Ag–0.5Cu–3Bi solder joint caused by EM phenomenon under the current density of 1.0×10^4 A/cm^2. However, a dual addition of Ni and Bi to the Sn–0.7Ag–0.5Cu effectively restrained the EM behaviors at high temperature aging (1.76×10^4 A/cm^2 at 25 and 120 °C for 58 h, 5.0×10^4 A/cm^2 at 150 °C for 1 min). This was probably because fusing Ni into Sn–0.7Ag–0.5Cu solder not only decreased the grain size but also increased the number of grain boundary, thus blocking the Cu diffusion [140]. Similarly, a multi-addition of 0.07 wt% Ni and 0.01 wt% Ge into Sn–3.5Ag–0.5Cu solder also caused a suppressive effect on Sn atom diffusion because of the combination of Ni with Sn as stable IMCs as well as the block of Ge distributing along grain boundaries [141]. Moreover, Ref. [142] reported that 1 wt% Zn addition could effectively suppressed the polarity effect on Sn–1Ag–0.5Cu solder joint induced by EM (DC density: 2×10^4 A/cm^2; T: 100 °C). This is due to the strong bonding between Zn and Cu atoms as Cu_5Zn_8 IMCs. Besides, Zn atoms were also observed to fill the vacancies left behind by Sn atom diffusion during the EM process, as shown in Fig. 24. So, the vacancy concentration at the cathode side could be counteracted, thus lowering the strength reduction in Zn-doped solder joint after electromigration with the evidence of fracture in the middle of the samples. However, brittle Ag_5Zn_8 instead of large amount of Ag_3Sn formed at the interface dramatically degraded the strength of the as-reflowed Sn–Ag–Cu solder joint. Therefore, this opposite strength results between strengthening and weakening repercussions caused by Zn addition remain to be further investigated.

Rare research has investigated the influence of RE addition on the microstructure evolution in the solder joint stressed with high density current. Xie et al. [134] once made a comparison of EM behaviors between Sn–3.9Ag–0.7Cu and Sn–3.9Ag–0.7Cu–0.5Ce solder joints under the average current density of 5×10^3 A/cm^2 at 100 °C. It was found that Cu diffusion induced by EM effect in the Ce-containing solder was accelerated, whereas rapid formation of Cu_6Sn_5 IMCs retarded pancake-type voids at the cathode side. However, $CeSn_3$ IMCs formed in the matrix could block the Sn diffusion, which was beneficial to inhibit EM phenomenon in Ce-containing solder. Also, the results of marker displacement and 3D void growth simulation indicated that Sn–Ag–Cu composites were demonstrated having higher EM resistance than Sn–Pb solder joint. Worthy of note is that current-induced Sn self-diffusion is the dominant failure mode at high temperature for Sn–3.9Ag–0.7Cu solder in this test, which can be expressed as follows:

$$\frac{J_{Cu}}{J_{Sn}} = 1.0 \times 10^{-4} \frac{Z^{*}_{\mathrm{Cu}}}{Z^{*}_{\mathrm{Sn}}} \exp\left(\frac{37.9\,(\mathrm{kJ/mol})}{kT}\right) \tag{8}$$

where Z^{*}_{Cu} and Z^{*}_{Sn} are the effective charge numbers of Cu in Sn and Sn in Sn, respectively, k and T are the Boltzmann

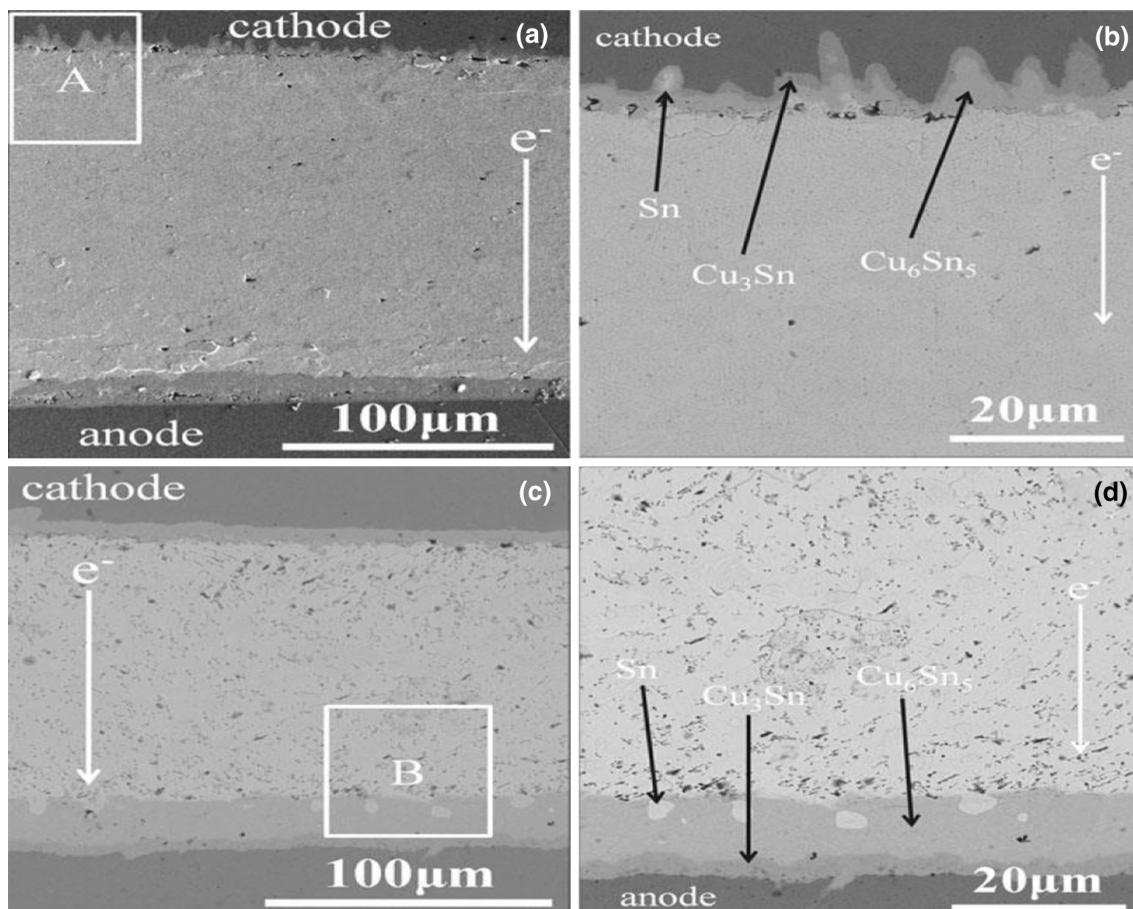

Fig. 23 SEM micrographs of Sn–3.0 Ag–0.5 Cu solder joint with current density of 10^4 A/cm^2 at 150 °C: **a**, **d** anode EM 1 and 3 days, respectively; **b**, **c** cathode EM for 1 and 3 days, respectively [139]

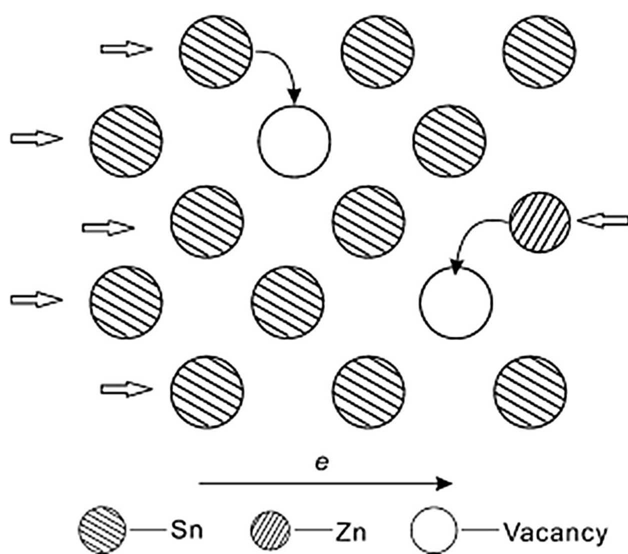

Fig. 24 The schematic diagram of the suppressed vacancy accumulation at the cathode side [142]

constant and the absolute temperature, respectively. Apparently, it reasonable to obtain that the EM flux ratio of Cu to Sn ($\frac{J_{Cu}}{J_{Sn}}$) is a function of temperature.

The influence of nanoparticles addition (e.g., Ni–CNTs [136], Al_2O_3 [143], La_2O_3 [17]) on the EM phenomenon was also studied by a few researchers. For instance, when exposed to current (current density: 1×10^4 A/cm^2), CNTs-doped Sn–3.5Ag–0.7Cu solder joints with excellent conductivity observed some high conductivity paths built for electrons to preferentially go through rather than collided with atoms in the solder. Consequently, EM phenomenon was effectively impeded with the result of only a small number of atoms moving from cathode towards anode, as demonstrated by two-dimensional (2D) finite element simulation (Fig. 25 [136]). Also, this simulation demonstrated that CNT has the current-carry capacity since the current density at the intermediate CNTs among the network reaches 10^6 A/cm^2, while that at region B (solder matrix) is only about 6×10^3 A/cm^2. So, it was evident to

obtain that the EM phenomenon was eventually weakened. Moreover, Sharma et al. [17] systematically studied the EM behaviors of Sn–3.0Ag–0.5Cu solder joints doped with various nanoparticles applying a self-designed test substrate under the conducting DC density of 1.4×10^3 A/mm^2 at 160 °C. The results showed that among all the examined composite solders, Sn–3.0Ag–0.5Cu solders containing 0.05 wt% La_2O_3, 0.05 wt% SiC and 0.5 wt% ZrO_2 were outstanding in resisting EM damages for no appreciable failures were detected in the direction of the electric current, and no larger void/cracks were observed at the cathode side. However, solder joints of Sn–3.0Ag–0.5Cu/Cu, Sn–3.0Ag–0.5Cu–0.05(Cu–CNT)/Cu and Sn–3.0Ag–0.5Cu–0.01Graphene/Cu all displayed large voids at the cathode side, which was presumably associated with both Sn and Cu atom diffusion. Even more serious was that local joule heating may be created by current crowding occurring at the neighboring Cu substrate caused by some voids at the cathode side. This may finally generate a temperature gradient that subsequently heat up the nearby solder and trigger an unceasing diffusion.

11 Sn whisker

Sn whisker, a conductive metal wire, generally buds and develops in RE-containing solder joints that can easily cause short circuit especially in today's high density electronic packages [71, 90]. The indispensable factors inducing Sn whisker in RE-containing Sn–Ag–Cu solders consists of sufficient Sn sources and compressive stresses. Generally, the origination of Sn sources is from the oxidation of Sn-RE phases (Sn - RE + O_2 → RE - O + Sn) or the nearby Sn diffusion. Whereas, the sources of compressive stresses are various, such as residual stresses in tin electroplatings, external mechanical stress and volume expansion induced by RE phase oxidation, IMCs growth and temperature alteration [90]. It was reported that one of the simplest methodology to avoid whisker issue was to spray the entire packaging structure with a thick coating [26]. Besides, it has been recently found that appropriate amount of Zn addition into Sn–Ag–Cu solders also has the capacity to inhibit Sn whisker growth. For instance, the growth rate of fiber-like Sn whisker extruding from Sn–3Ag–0.5Cu–1.0Ce solder surrounded by oxidized $CeSn_3$ will reach 1.2 Å/s with the elevation of storage temperature from 25 to 150 °C. However, neither lengthening nor coarsening of tin sprouts were detected in the Sn–9Zn–0.5Ce solder due to the formation of peritectic $(Ce_{0.8}Zn_{0.2})Sn_3$ IMCs with small size that can not only cut down the Sn sources, but can also relieve the compressive stress [27, 144]. Besides, with Ce content in Sn–3Ag–0.5Cu–1Ce decreasing down to 0.5 wt%, Zn addition (0.5 wt%) was also observed to inhibit the Sn whisker growth [145]. Xue et al. [146] recently claimed that an extra addition of Ga into Sn–9Zn−xNd can effectively prevent Sn whisker growth due to the formation of more stable GaNd and GaNd3 than SnNd. So, we argue that alloys that can substitute RE in Sn–RE phase or have more tendency to combine with RE than elemental Sn can be added into RE-containing solders to investigate whether they have positive effects on inhibiting Sn whisker growth.

Theoretical work besides morphology investigation is critically important to further understand Sn whisker growth mechanism in RE-containing solders. Broadly speaking, rare research has focused on this to date, which remains to be developed urgently in the future to thoroughly impede Sn whisker growth under various enviroments. Worthy of note is a classical successively compressive stress model, built by Chuang et al. [27, 147] for Sn whisker growth on the surface of RE-doped Sn–3Ag–0.5Cu solders, as shown in Fig. 26. Clearly, a thin pure tin layer, originating from the unoxidized tin atoms, inserts into the cerium oxide layer existing on the outer surface of the $CeSn_3$ precipitates. In this moment, large compressive stress, induced by volume expansion of thick oxide layer in $CeSn_3$, will squeeze the pure solder adjacent to the oxidized $CeSn_3$ phase to form hillocks (Fig. 26a). Subsequently, Sn–RE IMCs beneath the first Sn layer oxidize predominantly and release additional Sn atoms beneath the second RE-oxide layer. Consequently, the

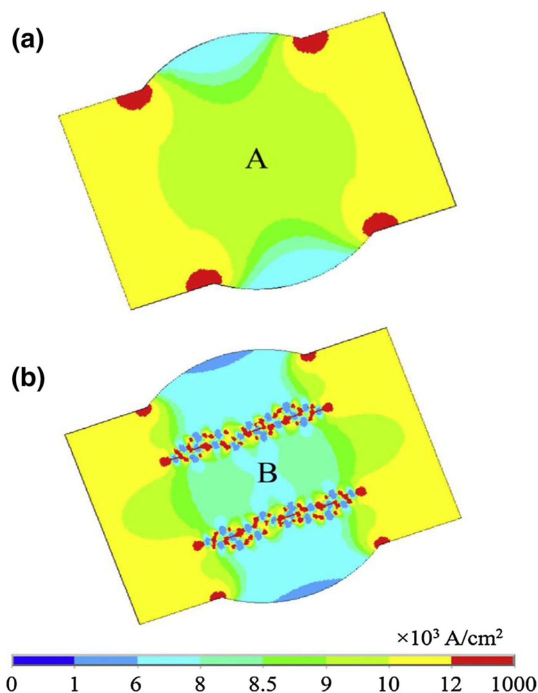

Fig. 25 Current density distribution in the: **a** Sn–3.5Ag–0.7Cu solder joint and **b** Sn–3.5Ag–0.7Cu–1Ni–CNT solder joint [136]

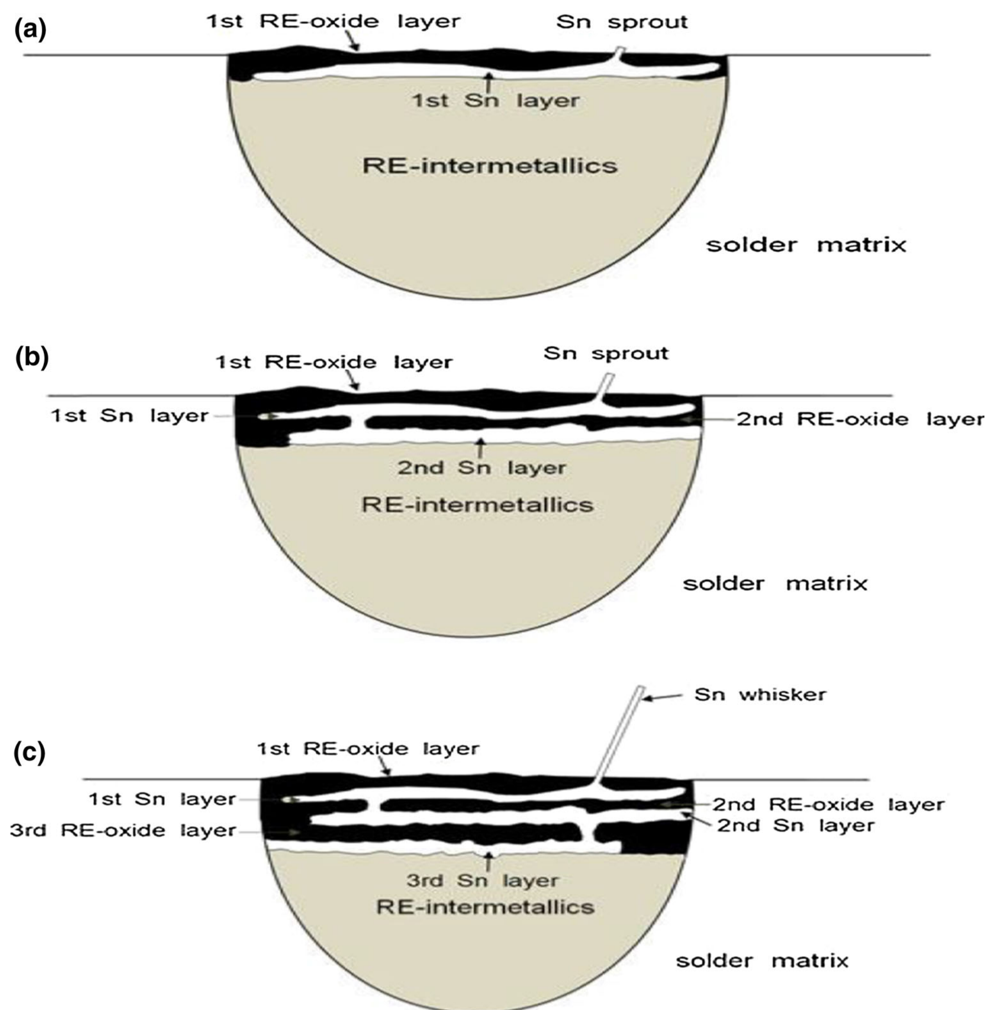

Fig. 26 The schematic diagram of successive compressive stress model built up for Sn whisker growth on the surface of RE-doped solders [147]

compressive stress can be further induced to extrude the pure Sn out of the first RE-oxide layer, as illustrated in Fig. 26b. Similarly, further oxidation of Sn–RE IMCs beneath the RE-oxide/Sn multilayer successively provide compressive stress as the driving force for continuous growth of Sn whiskers (Fig. 26c).

Factors affecting Sn whisker morphology are various. For instance, Figs. 27 and 28 [148] shows the different morphologies of Sn whisker in Sn–3.9Ag–0.7Cu–RE (2 wt% Ce, La, or Y) solders under two types of cooling conditions (water-quenched and furnace-cooled). Apparently, for water-quenched alloys, large and hillock-type whiskers isolated to areas directly adjacent to the $RESn_3$ particles were visibly detected on the specimen surface. However, for furnace-cooled alloys, it was the interior of IMCs rather than the particle-Sn matrix interface that observed the growth of needle-like or thread-like whiskers with longer length (smaller diameter). This morphology difference of Sn whiskers under two distinct cooling conditions is associated with different whiskering mechanisms, as shown in Fig. 29 [148]. As can be seen, small $RESn_3$ particles formed under water-quenched (Fig. 29a) created a relatively short diffusion pathway for Sn atoms to migrate simply towards the particle–matrix interface. Besides, Sn atoms can also diffuse into a neighboring Sn matrix from this interface. However, larger particles formed under furnace-cooled (Fig. 29b) might bring obstacles for Sn atoms to diffuse towards the particle–matrix boundaries. So, they generally diffuse away by developing RE–O phases and coalesce to create pure Sn phases with the formation of needle-like Sn whisker. Also, different metallographic cross sections as well as varied exposure areas of Sn–RE phase can also influence the morphology of Sn whiskers. For instance, for rosette-shape $NdSn_3$ phases in Sn–3Ag–0.5Cu–0.5Nd solder, four types of tin whiskers emerged on the surface of the oxidation $NdSn_3$ phases, as shown in Fig. 30 [147]. However, only two types of Sn whiskers (long fiber ones, diameter: 0.1–0.3 μm; short ones, diameter: >1 μm) were detected in $CeSn_3$ with cluster-shape formed in Sn–3Ag–0.5Cu–0.5Ce solder [149].

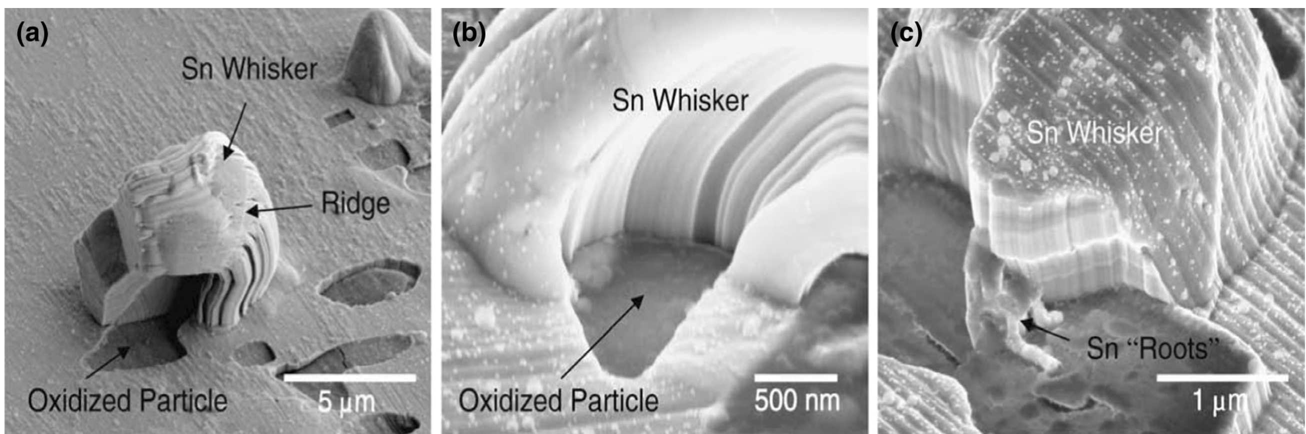

Fig. 27 High magnification SEM image of hillock-shape whiskers growing from the boundary between the $LaSn_3$ particle and Sn matrix in the water-quenched Sn–3.9Ag–0.7Cu–2La at 95 °C [148]

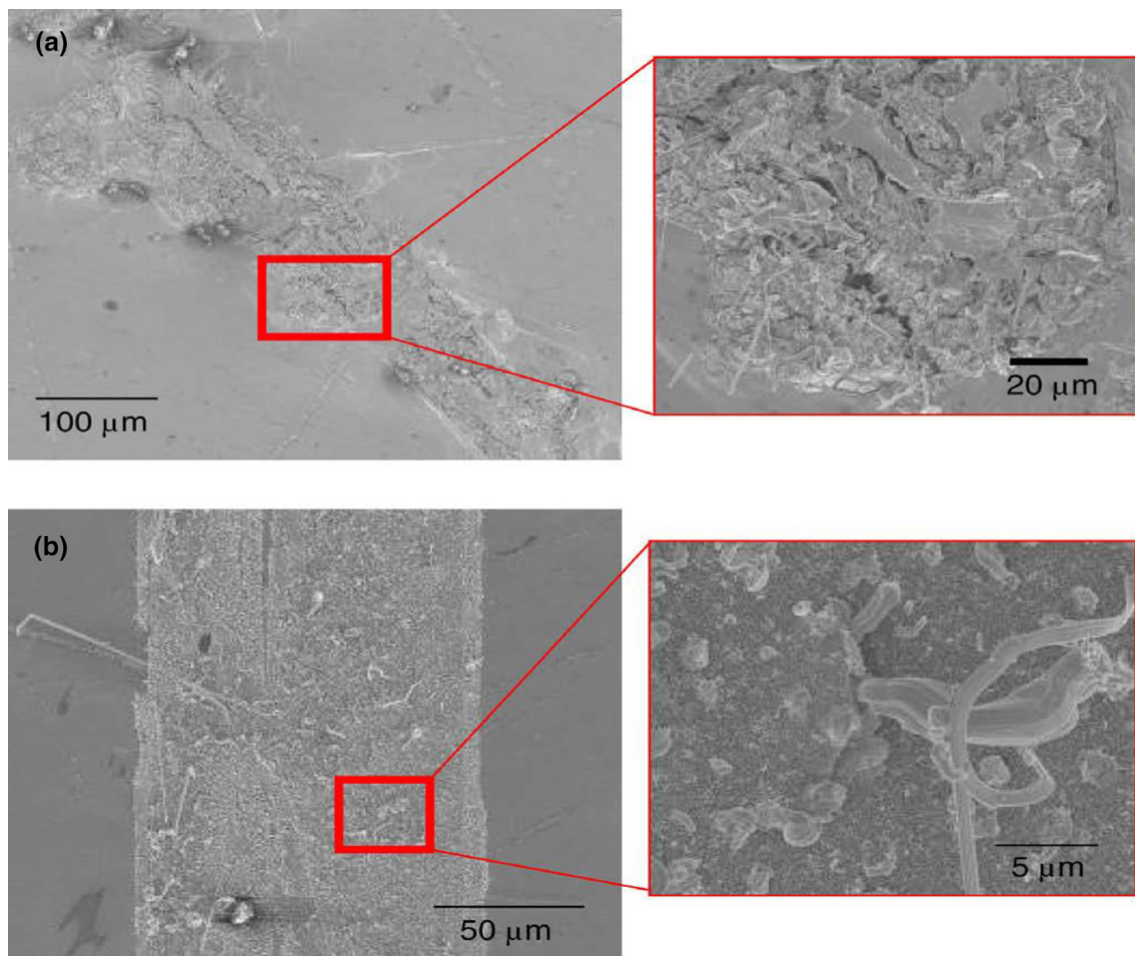

Fig. 28 SEM images of the microstructure of the surfaces of oxidized, furnace-cooled: **a** Sn–3.9Ag–0.7Cu–2La and **b** Sn–3.9Ag–0.7Cu–2Y after 1 year in air [148]

Other external factors such as NaCl solution, current density and fluxes types were also responsible for various behaviors of Sn whisker growth. For instance, Hua et al. [150] found that 3.5 wt% NaCl solution rapidly accelerated the growth and the lengthening of Sn whiskers in Sn–3.0Ag–0.5Cu–0.2In–3Zn solder with the growth rate and

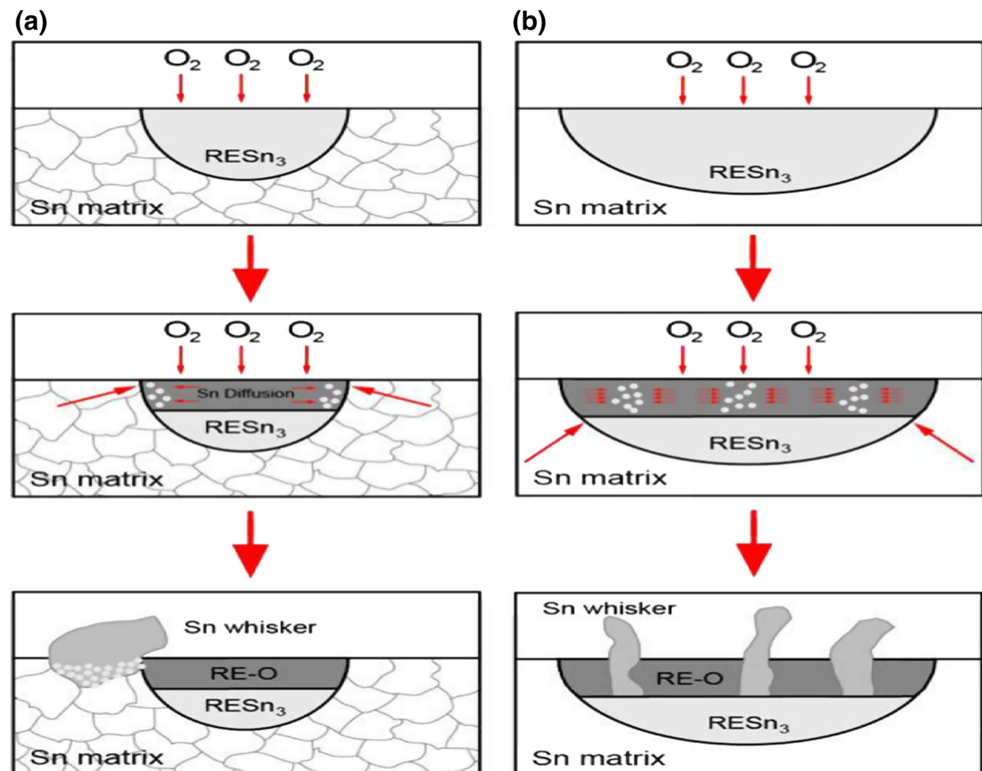

Fig. 29 The schematic diagram of the development and growth of Sn whiskers: **a** smaller Sn whiskers (water-quenched), **b** larger Sn whiskers (furnace-cooled) [148]

length approaching nearly to 5 Å/s and 300 μm, respectively. In addition, with the increase in stressed current density, Sn whisker growth could be evidently encouraged with the most substantial extent realized for 0.4 A/cm^2. Unexpectedly, a further rise in current density inhibited the whisker growth due to the relief of internal stress contributed by emerging porosities [151]. So, it is particularly essential to accurately measure out the danger zone of stressed current density to correctly guide the electronic engineer to design a series of secure soldering parameters. Furthermore, it was certified that anaerobic environment such as inert N_2 atmosphere and a halogen free flux like HBr activated fluxes could aid the suppression of Sn-oxides formation in Sn–3.0Ag–0.5Cu solder. Thus, the restraint of Sn whiskers in RE-containing solder became possible [152].

12 Conclusions

As is presented and analyzed above, the incorporation of alloy elements and nanoparticles to Sn–Ag–Cu solders has been fully demonstrated to be a feasible and effective method to overcome the limitations of original Sn–Ag–Cu solders and further modify series of solder properties. For instance, as for decreasing the T_m of Sn–Ag–Cu solders, optimal content of alloys like Ga (~30 °C), In (~157 °C), Bi (~271 °C), Zn (~420 °C) contribute more than other additives due to their inherent low-melting temperature. Besides, the development of low-melting nano-solder matching with suitable protection flux should be the focus of future research. In terms of narrowing down the melting range of Sn–Ag–Cu solders, we argue that the approach of higher decrement in T_L than that in T_S can best satisfy the industrial requirement. Additionally, when compared with nanoparticles addition, RE addition contributes more to wettability enhancement and microstructure refinement due to their surface-active quality. However, nanoparticles addition performs better in strengthening mechanical properties (e.g., microhardness, tensile strength, creep behaviors) mainly due to their higher capacity to effectively impede dislocation movements. In short, a full understanding of structure–property relationship influenced by foreign reinforcements is demanded to better their performance in electronic packages. Worthy of note is that the content of alloys (especially RE) and nanoparticles addition should be managed well or some reliability issues like Sn whisker and nanoparticles agglomeration may occur. Generally, the optimal range for RE addition is ascertained around 0.05 wt%, which can provide a better perspective or a rule-of-thumb to achieve the most satisfactory modification in various basic properties. However, the optimal range for nanoparticles addition is still unknown because of less experimental amount. Thus, to

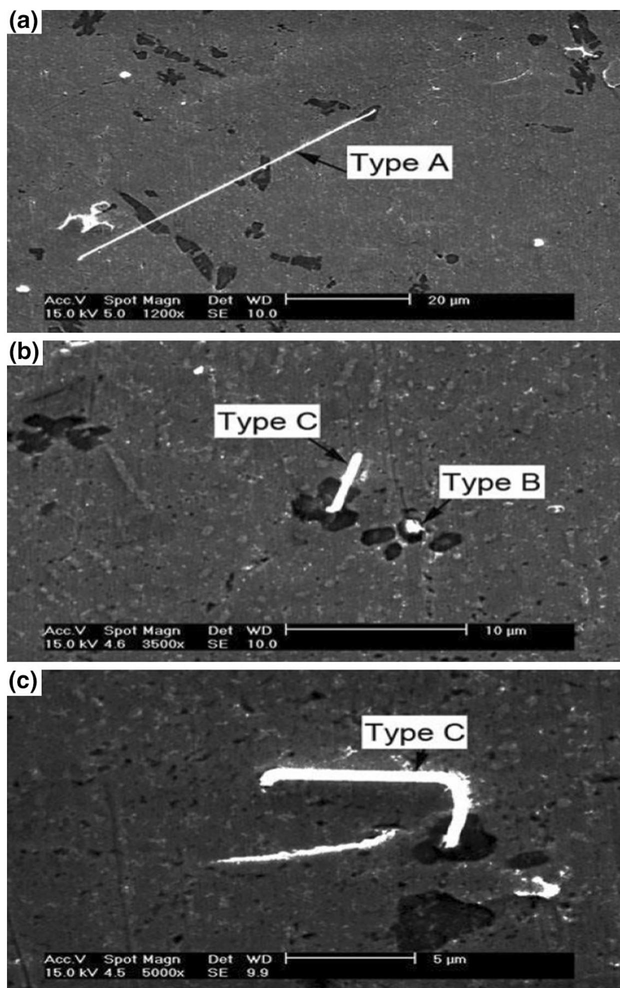

Fig. 30 Sn whisker growth with three types: A: long fiber, Type B: tiny sprout, and Type C: short fiber on the surface of Sn–3Ag–0.5Cu–0.5Nd solders (after air exposure at room temperature for 144 h) [147]

obtain the general optimal range for nanoparticles addition, massive experimental work still remains to be done. Moreover, in order to comprehensively evaluate the reliability of Sn–Ag–Cu solder joint, various forms of new reliability evaluation mechanisms can be made since reliability is determined by many factors, such as solder/substrate composition, soldering/reflowing parameters (temperature and time), external (thermo-) mechanical loading. Among them, temperature is an important soldering and storage index that should be controlled carefully in case of possible occurrence of mechanical and reliability degradation. Besides, with the continuous trend of miniaturization in electronic devices, the reliability issues of EM become more severe, which can be relieved by adding alloys that have similar radius as Cu (e.g., Co, Ni, Ge, Zn) or the current-carry nanoparticles (e.g., CNTs). However, research on TM phenomenon still stays at the initial stage of exploring TM behaviors in different solder systems such as Sn–Pb, Sn–Ag, Sn–Zn, Sn–Bi and Sn–Ag–Cu, so that massive experimental and theoretical work to investigate the influence of foreign alloys or nanoparticles addition should be underway. Besides, when analyzing atoms migration mechanisms, more complex conditions (e.g., EM, TM, back stresses, current crowding effect) should be taken into consideration to vividly mimic the complex stress condition of migration atoms. In terms of another reliability issue—Sn whisker in RE-containing solders, future focus should be shifted to analyzing their growth mechanisms rather than solely observing their growth behaviors to find out the most effective method to prevent its occurrence. Above all, this review concentrates more on uncovering the mechanisms hiding behind property modifications of Sn–Ag–Cu composite solders instead of simply listing the modified results, which has the value in providing a significant basis of excavating new idea and innovation on Sn–Ag–Cu solders.

Acknowledgments The Project (JSAWT-14-04) was supported by the Key Laboratory of Advanced Welding Technology of Jiangsu Province, China. This work was also supported by the Fundamental Research Funds for the Central Universities and the Foundation of Graduate Innovation Center in NUAA (Foundation No. kfjj20150604) and this work was also supported by the Priority Academic Program Development of Jiangsu Higher Education Institutions (PAPD).

References

1. L. Zhang, K.N. Tu, Structure and properties of lead-free solders bearing micro and nano particles. Mater. Sci. Eng. R **82**, 1–32 (2014)
2. M. Pecht, T. Shibutani, L. Wu, A reliability assessment guide for the transition planning to lead-free electronics for companies whose products are RoHS exempted or excluded. Microelectron. Reliab. (2016). doi:10.1016/j.microrel.2016.03.020
3. L.L. Gao et al., Effects of trace rare earth Nd addition on microstructure and properties of SnAgCu solder. J. Mater. Sci. Mater. Electron. **21**(7), 643–648 (2010)
4. J.W. Yoon, S.W. Kim, S.B. Jung, I.M.C. Morphology, Interfacial reaction and joint reliability of Pb-free Sn–Ag–Cu solder on electrolytic Ni BGA substrate. J. Alloys Compd. **392**(1), 247–252 (2005)
5. D.X. Luo, S.B. Xue, Z.Q. Li, Effects of Ga addition on microstructure and properties of Sn–0.5Ag–0.7Cu solder. J. Mater. Sci. Mater. Electron. **25**(8), 3566–3571 (2014)
6. S. Liu, S.B. Xue, P. Xue, D.X. Luo, Present status of Sn–Zn lead-free solders bearing alloying elements. J. Mater. Sci. Mater. Electron. **26**(7), 4389–4411 (2015)
7. A.E. Hammad, Evolution of microstructure, thermal and creep properties of Ni-doped Sn–0.5Ag–0.7Cu low-Ag solder alloys for electronic applications. Mater. Des. **52**, 663–670 (2013)
8. L. Sun, L. Zhang, Properties and microstructures of Sn–Ag–Cu–X lead-free solder joints in electronic packaging. Adv. Mater. Sci. Eng. **2015**, 1–16 (2015)
9. C.H. Chen et al., Interfacial reactions of low-melting Sn–Bi–Ga solder alloy on Cu substrate. J. Electron. Mater. **45**, 1–6 (2016)

10. G. Zeng, S.B. Xue, L. Zhang, L.L. Gao, A review on the interfacial intermetallic compounds between Sn–Ag–Cu based solders and substrates. J. Mater. Sci. Mater. Electron. **21**(5), 421–440 (2010)
11. A.T. Tan, A.W. Tan, F. Yusof, Influence of nanoparticle addition on the formation and growth of intermetallic compounds (IMCs) in Cu/Sn–Ag–Cu/Cu solder joint during different thermal conditions. Sci. Technol. Adv. Mater. (2016). doi:10.1088/1468-6996/16/3/033505
12. Y. Gu et al., Effect of nano-Fe_2O_3 additions on wettability and interfacial intermetallic growth of low-Ag content Sn–Ag–Cu solders on Cu substrates. J. Alloys. Compd. **627**, 39–47 (2015)
13. W.Y. Chen, C.Y. Yu, J.G. Duh, Improving the shear strength of Sn–Ag–Cu–Ni/Cu–Zn solder joints via modifying the microstructure and phase stability of Cu–Sn intermetallic compounds. Intermetallics **54**, 181–186 (2014)
14. N. Hamada et al., Effect of addition of small amount of zinc on microstructural evolution and thermal shock behavior in low-Ag Sn–Ag–Cu solder joints during thermal cycling. Mater. Trans. **54**(5), 796–805 (2013)
15. J.X. Wang, H. Nishikawa, Impact strength of Sn–3.0Ag–0.5Cu solder bumps during isothermal aging. Microelectron. Reliab. **54**(8), 1583–1591 (2014)
16. J.Y. Son et al., *Study on the Characteristics of Various Dopants in Sn-1Ag-0.8Cu Solder[C]//Electronics Packaging Technology Conference (EPTC)*, 2011 IEEE 13th IEEE, 231–235 (2011)
17. A. Sharma et al., Electromigration of composite Sn–Ag–Cu solder bumps. Electron. Mater. Lett. **11**(6), 1072–1077 (2015)
18. F.Y. Ouyang, C.L. Kao, In situ observation of thermomigration of Sn atoms to the hot end of 96.5Sn–3Ag–0.5Cu flip chip solder joints. J. Appl. Phys. **110**(12), 123525 (2011)
19. V.L. Niranjani et al., Influence of temperature and strain rate on tensile properties of single walled carbon nanotubes reinforced Sn–Ag–Cu lead free solder alloy composites. Mater. Sci. Eng. A **529**, 257–264 (2011)
20. Q.K. Zhang et al., Effects of Ga addition on microstructure and properties of Sn–Ag–Cu/Cu solder joints. J. Alloys Compd. **622**, 973–978 (2015)
21. A.E. Hammad, A.M. El-Taher, Mechanical deformation behavior of Sn–Ag–Cu solders with minor addition of 0.05 wt% Ni. J. Electron. Mater. **43**(11), 4146–4157 (2014)
22. L. Zhang et al., Properties and microstructures of SnAgCu–xEu alloys for concentrator silicon solar cells solder layer. Sol. Energy Mater. Sol. C **130**, 397–400 (2014)
23. M. Yang et al., Effects of Ag content on the interfacial reactions between liquid Sn–Ag–Cu solders and Cu substrates during soldering. J. Alloys Compd. (2016). doi:10.1016/j.jallcom.2016.03.177
24. L.W. Lin et al., Alloying modification of Sn–Ag–Cu solders by manganese and titanium. Microelectron. Reliab. **49**(3), 235–241 (2009)
25. L.L. Gao et al., Effect of praseodymium on the microstructure and properties of Sn3.8Ag0.7Cu solder. J. Mater. Sci. Mater. Electron. **21**(9), 910–916 (2010)
26. A.T. Wu, Y.C. Ding, The suppression of tin whisker growth by the coating of tin oxide nano particles and surface treatment. Microelectron. Reliab. **49**(3), 318–322 (2009)
27. T.H. Chuang, H.J. Lin, Inhibition of whisker growth on the surface of Sn–3Ag–0.5Cu–0.5Ce solder alloyed with Zn. J. Electron. Mater. **38**(3), 420–424 (2009)
28. L.M. Yang, Z.F. Zhang, Effects of Y_2O_3 nanoparticles on growth behaviors of Cu_6Sn_5 grains in soldering reaction. J. Electron. Mater. **42**(12), 3552–3558 (2013)
29. I. Shafiq, H.Y. Lau, Y.C. Chan, Effect of trace diamond nanoparticle addition on the interfacial, mechanical, and damping properties of Sn–3.0Ag–0.5Cu solder alloy. J. Electron. Mater. **42**(9), 2835–2847 (2013)
30. Y. Tang, Y.C. Pan, G.Y. Li, Influence of TiO_2 nanoparticles on thermal property, wettability and interfacial reaction in Sn–3.0Ag–0.5Cu–xTiO_2 composite solder. J. Mater. Sci. Mater. Electron. **24**(5), 1587–1594 (2013)
31. A. Fawzy et al., Effect of ZnO nanoparticles addition on thermal, microstructure and tensile properties of Sn–3.5Ag–0.5Cu (SAC355) solder alloy. J. Mater. Sci. Mater. Electron. **24**(9), 3210–3218 (2013)
32. S. Xu et al., Interfacial intermetallic growth and mechanical properties of carbon nanotubes reinforced Sn3.5Ag0.5Cu solder joint under current stressing. J. Alloys Compd. **595**, 92–102 (2014)
33. A.A. El-Daly et al., Microstructural modifications and properties of SiC nanoparticles-reinforced Sn–3.0Ag–0.5Cu solder alloy. Mater. Des. **65**, 1196–1204 (2015)
34. A. Haseeb, M.M. Arafat, M.R. Johan, Stability of molybdenum nanoparticles in Sn–3.8Ag–0.7Cu solder during multiple reflow and their influence on interfacial intermetallic compounds. Mater. Charact. **64**, 27–35 (2012)
35. L.C. Tsao et al., Effects of nano-Al_2O_3 additions on microstructure development and hardness of Sn3.5Ag0.5Cu solder. Mater. Des. **31**(10), 4831–4835 (2010)
36. S. Chellvarajoo, M.Z. Abdullah, C.Y. Khor, Effects of diamond nanoparticles reinforcement into lead-free Sn–3.0Ag–0.5Cu solder pastes on microstructure and mechanical properties after reflow soldering process. Mater. Des. **82**, 206–215 (2015)
37. H.R. Kotadia, P.D. Howes, S.H. Mannan, A review: on the development of low melting temperature Pb-free solders. Microelectron. Reliab. **54**(6), 1253–1273 (2014)
38. A.A. El-Daly et al., Thermal analysis and mechanical properties of Sn–1.0Ag–0.5Cu solder alloy after modification with SiC nano-sized particles. J. Mater. Sci. Mater. Electron. **24**(8), 2976–2988 (2013)
39. D.X. Luo, S.B. Xue, S. Liu, Investigation on the intermetallic compound layer growth of Sn–0.5Ag–0.7Cu–xGa/Cu solder joints during isothermal aging. J. Mater. Sci. Mater. Electron. **25**(12), 5195–5200 (2014)
40. A.A. El-Daly, A.M. El-Taher, S. Gouda, Novel Bi-containing Sn–1.5Ag–0.7Cu lead-free solder alloy with further enhanced thermal property and strength for mobile products. Mater. Des. **65**, 796–805 (2015)
41. C. Lejuste, F. Hodaj, L. Petit, Solid state interaction between a Sn–Ag–Cu–In solder alloy and Cu substrate. Intermetallics **36**, 102–108 (2013)
42. A.A. El-Daly, A.M. El-Taher, Evolution of thermal property and creep resistance of Ni and Zn-doped Sn–2.0Ag–0.5Cu lead-free solders. Mater. Des. **51**, 789–796 (2013)
43. A.A. El-Daly et al., Influence of Zn addition on the microstructure, melt properties and creep behavior of low Ag-content Sn–Ag–Cu lead-free solders. Mater. Sci. Eng. A **608**, 130–138 (2014)
44. C.L. Chuang et al., Effects of small amount of active Ti element additions on microstructure and property of Sn3.5Ag0.5Cu solder. Mater. Sci. Eng. A **558**, 478–484 (2012)
45. D.A.A. Shnawah et al., Microstructure, mechanical, and thermal properties of the Sn–1Ag–0.5Cu solder alloy bearing Fe for electronics applications. Mater. Sci. Eng. A **551**, 160–168 (2012)
46. L.L. Gao et al., Effect of alloying elements on properties and microstructures of SnAgCu solders. Microelectron. Eng. **87**(11), 2025–2034 (2010)
47. M.A. Dudek, N. Chawla, Effect of rare-earth (La, Ce, and Y) additions on the microstructure and mechanical behavior of Sn–

3.9Ag–0.7Cu solder alloy. Metall. Mater. Trans. A **41**(3), 610–620 (2010)
48. X.D. Liu et al., Effect of graphene nanosheets reinforcement on the performance of SnAgCu lead-free solder. Mater. Sci. Eng. A **562**, 25–32 (2013)
49. Y.D. Han et al., Development of a Sn–Ag–Cu solder reinforced with Ni-coated carbon nanotubes. J. Mater. Sci. Mater. Electron. **22**(3), 315–322 (2011)
50. S. Chantaramanee et al., Development of a lead-free composite solder from Sn–Ag–Cu and Ag-coated carbon nanotubes. J. Mater. Sci. Mater. Electron. **24**(10), 707–3715 (2013)
51. A.A. El-Daly et al., Novel SiC nanoparticles-containing Sn–1.0Ag–0.5Cu solder with good drop impact performance. Mater. Sci. Eng. A **578**, 62–71 (2013)
52. K.C. Yung et al., Size control and characterization of Sn–Ag–Cu lead-free nanosolders by a chemical reduction process. J. Electron. Mater. **41**(2), 313–321 (2012)
53. F.E. Atalay et al., Nanowires of lead-free solder alloy SnCuAg. J. Nanomater. **2011**, 37 (2011)
54. A. Novikov, G. Holzhüter, M. Nowottnick. *Low-Temperature Assembling Process with Nanoscaled Solder Layers[C]//Nanotechnology (IEEE-NANO)*, 2012 12th IEEE Conference on IEEE, 1–4 (2012)
55. Y. Shu et al., Synthesis and thermal properties of low melting temperature tin/indium (Sn/In) lead-free nanosolders and their melting behavior in a vapor flux. J. Alloys Compd. **626**, 391–400 (2015)
56. A.A. El-Daly et al., Microstructure, mechanical properties, and deformation behavior of Sn–1.0Ag–0.5Cu solder after Ni and Sb additions. Mater. Des. **43**, 40–49 (2013)
57. A.A. El-Daly, A.E. Hammad, Enhancement of creep resistance and thermal behavior of eutectic Sn–Cu lead-free solder alloy by Ag and In-additions. Mater. Des. **40**, 292–298 (2012)
58. A.A. El-Daly, A.M. El-Taher, T.R. Dalloul, Improved creep resistance and thermal behavior of Ni-doped Sn–3.0Ag–0.5Cu lead-free solder. J. Alloys Compd. **587**, 32–39 (2014)
59. M. Amagai, A study of nanoparticles in Sn–Ag based lead free solders. Microelectron. Reliab. **48**(1), 1–16 (2008)
60. L. Zhang et al., Properties enhancement of SnAgCu solders containing rare earth Yb. Mater. Des. **57**, 646–651 (2014)
61. Z. Deng, Y. Qian, Effect of P on the oxidation resistance of Sn–0.7Cu lead-free solder. Electron. Process. Technol. **4**, 000 (2006)
62. X.J. Wang et al., Effect of doping Al on the liquid oxidation of Sn–Bi–Zn solder. J. Mater. Sci. Mater. Electron. **25**(5), 2297–2304 (2014)
63. W.X. Dong et al., Effects of small amounts of Ni/P/Ce element additions on the microstructure and properties of Sn3.0Ag0.5Cu solder alloy. J. Mater. Sci. Mater. Electron. **20**(10), 1008–1017 (2009)
64. J. J. Wang et al., Study on low silver Sn–Ag–Cu–P alloy for wave soldering physical and failure analysis of integrated circuits (IPFA), 2013 20th IEEE International Symposium on the IEEE, 485–489 (2013)
65. L. Hua et al., *Effects of Zn, Ge Doping on Electrochemical Migration, Oxidation Characteristics and Corrosion Behavior of Lead-Free Sn–3.0Ag–0.5Cu Solder for Electronic Packaging[C]//Electronic Packaging Technology & High Density Packaging (ICEPT-HDP)*, 2010 11th International Conference on IEEE, 1151–1157 (2010)
66. A.J. Jeon et al., Effect of indium content on the melting point, dross, and oxidation characteristics of Sn–2Ag–3Bi–xIn Solders. J. Electron. Packag. **135**(2), 021006 (2013)
67. M.A. Dudek, N. Chawla, Oxidation behavior of rare-earth-containing Pb-free solders. J. Electron. Mater. **38**(2), 210–220 (2009)
68. D. Bonn et al., Wetting and spreading. Rev. Mod. Phys. **81**(2), 739 (2009)
69. M.E. Loomans et al., Investigation of multi-component lead-free solders. J. Electron. Mater. **23**(8), 741–746 (1994)
70. W.F. Feng, C.Q. Wang, M. Morinaga, Electronic structure mechanism for the wettability of Sn-based solder alloys. J. Electron. Mater. **31**(3), 185–190 (2002)
71. G. Zeng et al., Recent advances on Sn–Cu solders with alloying elements: review. J. Mater. Sci. Mater. Electron. **22**(6), 565–578 (2011)
72. W.X. Chen et al., Effects of rare earth Ce on properties of Sn–9Zn lead-free solder. J. Mater. Sci. Mater. Electron. **21**(7), 719–725 (2010)
73. H.W. Zhang, F.L. Sun, Y. Liu, *Effects of Adding Some Elements on Solderability of Sn–0.7 Ag–0.5 Cu Solder[C]//Electronic Packaging Technology & High Density Packaging (ICEPT-HDP)*, 2010 11th International Conference on IEEE, 254–257 (2010)
74. S. Lu et al., The effects of Bi on physical and microstructural characteristics of Sn–Ag–Cu lead-free solders[C]//physical and failure analysis of integrated circuits, 2009. IPFA 2009. 16th IEEE international symposium on the IEEE, 782–784 (2009)
75. Y. Li et al., Effect of TiO_2 addition concentration on the wettability and intermetallic compounds growth of Sn3.0Ag0.5Cu–xTiO_2 nano-composite solders. J. Mater. Sci. Mater. Electron. **25**(9), 3816–3827 (2014)
76. L. Bernstein, Semiconductor joining by the solid–liquid-interdiffusion (SLID) process I. The systems Ag–In, Au–In, and Cu–In. J. Electrochem. Soc. **113**(12), 1282–1288 (1966)
77. L. Yang et al., Effect of $BaTiO_3$ on the microstructure and mechanical properties of Sn1.0Ag0.5Cu lead-free solder. J. Mater. Sci. Mater. Electron. **26**(1), 613–619 (2015)
78. M.J. Rizvi et al., Wetting and reaction of Sn–2.8Ag–0.5Cu–1.0Bi solder with Cu and Ni substrates. J. Electron. Mater. **34**(8), 1115–1122 (2005)
79. X.J. Liu et al., Thermodynamic calculation of phase equilibria in the Sn–Ag–Cu–Ni–Au system. J. Electron. Mater. **36**(11), 1429–1441 (2007)
80. K.S. Kim, S.H. Huh, K. Suganuma, Effects of intermetallic compounds on properties of Sn–Ag–Cu lead-free soldered joints. J. Alloys Compd. **352**(1), 226–236 (2003)
81. S.K. Kang et al., Ag_3Sn plate formation in the solidification of near-ternary eutectic Sn–Ag–Cu. JOM **55**(6), 61–65 (2003)
82. L. Yang, Z.F. Zhang, Growth behavior of intermetallic compounds in Cu/Sn3.0Ag0.5Cu solder joints with different rates of cooling. J. Electron. Mater. **44**(1), 590–596 (2015)
83. N.Y. Chen, *Bond-parametric function and its applications* (Science Press, Peking, 1976), p. 15
84. D.A. Shnawah et al., Study on coarsening of Ag_3Sn intermetallic compound in the Fe-modified Sn–1Ag–0.5Cu solder alloys. J. Alloys Compd. **622**, 184–188 (2015)
85. L.S. Darken, R.W. Gurry, *Physical chemistry of metals[M]* (McGraw-Hill, New York, 1953)
86. X. Chen et al., Microstructures and mechanical properties of Sn–0.1Ag–0.7Cu–(Co, Ni, and Nd) lead-free solders. J. Electron. Mater. **44**(2), 725–732 (2015)
87. A.A. El-Daly, A.M. El-Taher, S. Gouda, Development of new multicomponent Sn–Ag–Cu–Bi lead-free solders for low-cost commercial electronic assembly. J. Alloys Compd. **627**, 268–275 (2015)
88. A.A. El-Daly et al., Microstructural modifications and properties of low-Ag-content Sn–Ag–Cu solder joints induced by Zn alloying. J. Alloys Compd. **653**, 402–410 (2015)
89. S.Y. Xu et al., Effects of FeCo magnetic nanoparticles on microstructure of Sn–Ag–Cu alloys. J. Appl. Phys. **113**(17), 17A301 (2013)

90. K.N. Tu, Irreversible processes of spontaneous whisker growth in bimetallic Cu–Sn thin-film reactions. Phys. Rev. B **49**(3), 2030 (1994)
91. K.N. Tu, R.D. Thompson, Kinetics of interfacial reaction in bimetallic Cu–Sn thin films. Acta Metall. **30**(5), 947–952 (1982)
92. L. Zhang et al., Interface reaction between SnAgCu/SnAgCuCe solders and Cu substrate subjected to thermal cycling and isothermal aging. J. Alloys Compd. **510**(1), 38–45 (2012)
93. S.Y. Chang et al., The morphology and kinetic evolution of intermetallic compounds at Sn–Ag–Cu solder/Cu and Sn–Ag–Cu–0.5Al_2O_3 composite solder/Cu interface during soldering reaction. J. Mater. Sci. Mater. Electron. **23**(1), 100–107 (2012)
94. T. Fouzder et al., Influence of $SrTiO_3$ nano-particles on the microstructure and shear strength of Sn–Ag–Cu solder on Au/Ni metallized Cu pads. J. Alloys Compd. **509**(5), 1885–1892 (2011)
95. J.F. Li, P.A. Agyakwa, C.M. Johnson, Effect of trace Al on growth rates of intermetallic compound layers between Sn-based solders and Cu substrate. J. Alloys Compd. **545**, 70–79 (2012)
96. C.E. Ho et al., Influence of Pd concentration on the interfacial reaction and mechanical reliability of the Ni/Sn–Ag–Cu–xPd System. J. Electron. Mater. **41**(1), 2–10 (2012)
97. G.Y. Li et al., Influence of dopant on growth of intermetallic layers in Sn–Ag–Cu solder joints. J. Electron. Mater. **40**(2), 165–175 (2011)
98. A.A. El-Daly, A.M. El-Taher, Improved strength of Ni and Zn-doped Sn–2.0Ag–0.5Cu lead-free solder alloys under controlled processing parameters. Mater. Des. **47**(9), 607–614 (2013)
99. A.K. Gain et al., Effect of small Sn–3.5Ag–0.5Cu additions on the structure and properties of Sn–9Zn solder in ball grid array packages. Microelectron. Eng. **86**(11), 2347–2353 (2009)
100. J. Keller et al., Mechanical properties of Pb-free SnAg solder joints. Acta Mater. **59**(7), 2731–2741 (2011)
101. L.M. Yang, Z.F. Zhang, Effect of Y_2O_3 nanoparticles addition on the microstructure and tensile strength of Cu/Sn3.0Ag0.5Cu solder joint. J. Appl. Phys. **117**(1), 015308 (2015)
102. A.K. Gain, Y.C. Chan, W.K.C. Yung, Effect of additions of ZrO_2 nano-particles on the microstructure and shear strength of Sn–Ag–Cu solder on Au/Ni metallized Cu pads. Microelectron. Reliab. **51**(12), 2306–2313 (2011)
103. L.C. Tsao et al., Effects of nano-Al_2O_3 particles on microstructure and mechanical properties of Sn3.5Ag0.5Cu composite solder ball grid array joints on Sn/Cu pads. Mater. Des. **50**, 774–781 (2013)
104. Y. Liu, F.L. Sun, X.M. Li, Effect of Ni, Bi concentration on the microstructure and shear behavior of low-Ag SAC–Bi–Ni/Cu solder joints. J. Mater. Sci. Mater. Electron. **25**(6), 2627–2633 (2014)
105. D.A.A. Shnawah et al., The bulk alloy microstructure and mechanical properties of Sn–1Ag–0.5Cu–xAl solders (x = 0, 0.1 and 0.2 wt%). J. Mater. Sci. Mater. Electron. **23**(11), 1988–1997 (2012)
106. A.E. Hammad, Investigation of microstructure and mechanical properties of novel Sn–0.5Ag–0.7Cu solders containing small amount of Ni. Mater. Des. **50**(17), 108–116 (2013)
107. A.A. El-Daly et al., Properties enhancement of low Ag-content Sn–Ag–Cu lead-free solders containing small amount of Zn. J. Alloys Compd. **614**, 20–28 (2014)
108. V.L. Niranjani et al., Creep behaviour of SAC387 lead free solder alloy reinforced with single walled carbon nanotubes. Trans. Indian Met. **68**(2), 311–317 (2015)
109. A.A. El-Daly et al., Tensile deformation behavior and melting property of nano-sized ZnO particles reinforced Sn–3.0Ag–0.5Cu lead-free solder. Mater. Sci. Eng. A **618**, 389–397 (2014)
110. A.A. El-Daly, A.M. El-Taher, T.R. Dalloul, Enhanced ductility and mechanical strength of Ni-doped Sn–3.0Ag–0.5Cu lead-free solders. Mater. Des. **55**, 309–318 (2014)
111. Y. Lee, C. Basaran, A creep model for solder alloys. J. Electron. Packag. **133**(4), 044501 (2011)
112. D. Witkin, Creep behavior of Bi-containing lead-free solder alloys. J. Electron. Mater. **41**(2), 190–203 (2012)
113. Y.D. Han et al., Creep mitigation in Sn–Ag–Cu composite solder with Ni-coated carbon nanotubes. J. Mater. Sci. Mater. Electron. **23**(5), 1108–1115 (2011)
114. Z.B. Yang, W. Zhou, P. Wu, Effects of Ni-coated carbon nanotubes addition on the microstructure and mechanical properties of Sn–Ag–Cu solder alloys. Mater. Sci. Eng. A **590**, 295–300 (2014)
115. F.X. Che, X. Zhang, J.K. Lin, Reliability study of 3D IC packaging based on through-silicon interposer (TSI) and silicon-less interconnection technology (SLIT) using finite element analysis. Microelectron. Reliab. (2016). doi:10.1016/j.microrel.2015.12.041
116. C.S. Lau et al., Thermo-mechanical challenges of reflowed lead-free solder joints in surface mount components: a review. Solder. Surf. Mt. Technol. **28**(2), 41–62 (2016)
117. Q. Zhou et al., Microstructural evolution of SAC305 solder joints in wafer level chip-scale packaging (WLCSP) with continuous and interrupted accelerated thermal cycling. J. Electron. Mater. **45**(6), 1–12 (2016)
118. L. Zhang et al., Microstructures and fatigue life of SnAgCu solder joints bearing nano-Al particles in QFP devices. Electron. Mater. Lett. **10**(3), 645–647 (2014)
119. M.A. Matin, W.P. Vellinga, M.G.D. Geers, Thermomechanical fatigue damage evolution in SAC solder joints. Mater. Sci. Eng. A **445**, 73–85 (2007)
120. F.X. Che, J.H.L. Pang, Characterization of IMC layer and its effect on thermomechanical fatigue life of Sn–3.8Ag–0.7Cu solder joints. J. Alloys Compd. **541**, 6–13 (2012)
121. S. Mukherjee, T.T. Mattila, A. Dasgupta, *Effect of Addition of Manganese and Antimony on Viscoplastic Properties and Cyclic Mechanical Durability of Low Silver Sn–Ag–Cu solder[C]// Thermal and Thermomechanical Phenomena in Electronic Systems (ITherm)*, 2012 13th IEEE Intersociety Conference on IEEE, 888–895 (2012)
122. Y.D. Han et al., Interfacial reaction and shear strength of Ni-coated carbon nanotubes reinforced Sn–Ag–Cu solder joints during thermal cycling. Intermetallics **31**, 72–78 (2012)
123. D.A. Shnawah, M.F.M. Sabri, I.A. Badruddin, A review on thermal cycling and drop impact reliability of SAC solder joint in portable electronic products. Microelectron. Reliab. **52**(1), 90–99 (2012)
124. A.M. Yu et al., Pd-doped Sn–Ag–Cu–In solder material for high drop/shock reliability. Mater. Res. Bull. **45**(3), 359–361 (2010)
125. K. Lee, K.S. Kim, K. Suganuma, Influence of indium addition on electromigration behavior of solder joint. J. Mater. Res. **26**(20), 2624–2631 (2011)
126. Q.T. Huynh et al., Electromigration in eutectic Sn–Pb solder lines. J. Appl. Phys. **89**(8), 4332–4335 (2001)
127. X. Zhu et al., Electromigration in Sn–Ag solder thin films under high current density. Thin Solid Films **565**(9), 193–201 (2014)
128. F. Su et al., Study of electromigration-induced stress of solder. J. Electron. Packag. **137**(2), 021006 (2015)
129. C. Chen, H.M. Tong, K.N. Tu, Electromigration and thermomigration in Pb-free flip-chip solder joints. Annu. Rev. Mater. Res. **40**, 531–555 (2010)
130. W. Yao, C. Basaran, Computational damage mechanics of electromigration and thermomigration. J. Appl. Phys. **114**(10), 103708 (2013)
131. K.N. Tu, H.Y. Hsiao, C. Chen, Transition from flip chip solder joint to 3D IC microbump: its effect on microstructure anisotropy. Microelectron. Reliab. **53**(1), 2–6 (2013)

132. Y. Tao et al., *Theoretical Analysis on the Element Diffusion During Thermomigration[C]//Electronic Packaging Technology and High Density Packaging (ICEPT-HDP)*, 2011 12th International Conference on IEEE, 1–5 (2011)
133. H.B. Huntington, A.R. Grone, Current-induced marker motion in gold wires. J. Phys. Chem. Solids **20**(1), 76–87 (1961)
134. H.X. Xie et al., Electromigration damage characterization in Sn–3.9Ag–0.7Cu and Sn–3.9Ag–0.7Cu–0.5Ce solder joints by three-dimensional X-ray tomography and scanning electron microscopy. J. Electron. Mater. **43**(1), 33–42 (2014)
135. K. Zeng, K.N. Tu, Six cases of reliability study of Pb-free solder joints in electronic packaging technology. Mater. Sci. Eng. R **38**(2), 55–105 (2002)
136. Z. Yang, W. Zhou, P. Wu, Effects of Ni-coated carbon nanotubes addition on the electromigration of Sn–Ag–Cu solder joints. J. Alloys Compd. **581**, 202–205 (2013)
137. Z.H.A.O. Ni et al., Research progress in thermomigration of metal atoms in micro solder joints and its effect on interfacial reaction. Chin. J. Nonferr. Met. **25**(8), 2157–2166 (2015)
138. S.H. Lee, C.M. Chen, Electromigration in a Sn–3 wt% Ag–0.5 wt% Cu–3 wt% Bi solder stripe between two Cu electrodes under current stressing. J. Electron. Mater. **40**(9), 1943–1949 (2011)
139. L. Ma et al., Effects of Co additions on electromigration behaviors in Sn–3.0Ag–0.5Cu-based solder joint. J. Mater. Sci. **46**(14), 4896–4905 (2011)
140. F.L. Sun, Y. Liu, J.B. Wang, *Improving the Solderability and Electromigration Behavior of Low-Ag SnAgCu Soldering[C]// Thermal, Mechanical and Multi-Physics Simulation and Experiments in Microelectronics and Microsystems (EuroSimE)*, 2011 12th International Conference on IEEE, 1/5–5/5 (2011)
141. X. Zhao et al., The effect of adding Ni and Ge microelements on the electromigration resistance of low-Ag based SnAgCu solder. Microsyst. Technol. **18**(12), 2077–2084 (2012)
142. H.Y. Liu et al., Effects of Zn addition on electromigration behavior of Sn–1Ag–0.5Cu solder interconnect. J. Mater. Sci. Mater. Electron. **24**(1), 211–216 (2013)
143. P. He et al., *Effect of 0.8 wt% Al_2O_3 Nanoparticles Addition on the Microstructures and Electromigration Behavior of Sn–Ag–Cu Solder Joint[C]//Electronic Packaging Technology (ICEPT)*, 2015 16th International Conference on IEEE, 1014–1017 (2015)
144. T.H. Chuang, Rapid whisker growth on the surface of Sn–3Ag–0.5Cu–1.0Ce solder joints. Scr. Mater. **55**(11), 983–986 (2006)
145. H.J. Lin, T.H. Chuang, Effects of Ce and Zn additions on the microstructure and mechanical properties of Sn–3Ag–0.5Cu solder joints. J. Alloys Compd. **500**(2), 167–174 (2010)
146. P. Xue et al., Inhibiting the growth of Sn whisker in Sn–9Zn lead-free solder by Nd and Ga. J. Mater. Sci. Mater. Electron. **25**(6), 2671–2675 (2014)
147. T.H. Chuang, C.C. Jain, Morphology of the Tin whiskers on the surface of a Sn–3Ag–0.5Cu–0.5Nd Alloy. Metall. Mater. Trans. A **42**(3), 684–691 (2010)
148. M.A. Dudek, N. Chawla, Mechanisms for Sn whisker growth in rare earth-containing Pb-free solders. Acta Mater. **57**(15), 4588–4599 (2009)
149. T.H. Chuang, S.F. Yen, Abnormal growth of tin whiskers in a Sn3Ag0.5Cu0.5Ce solder ball grid array package. J. Electron. Mater. **35**(8), 1621–1627 (2006)
150. L. Hua, C. Yang, Corrosion behavior, whisker growth, and electrochemical migration of Sn–3.0Ag–0.5 Cu solder doping with In and Zn in NaCl solution. Microelectron. Reliab. **51**(12), 2274–2283 (2011)
151. A. Sharma et al., Influence of current density on microstructure of pulse electrodeposited tin coatings. Mater. Charact. **68**, 22–32 (2012)
152. A. Baated et al., Effects of reflow atmosphere and flux on Sn whisker growth of Sn–Ag–Cu solders. J. Mater. Sci. Mater. Electron. **21**(10), 1066–1075 (2010)